
Article:
Al-Neama, AF, Kapur, N orcid.org/0000-0003-1041-8390, Summers, J orcid.org/0000-0001-8266-5038 et al. (1 more author) (2018) Thermal management of GaN HEMT devices using serpentine minichannel heat sinks. Applied Thermal Engineering, 140. pp. 622-636. ISSN 1359-4311

https://doi.org/10.1016/j.applthermaleng.2018.05.072

Thermal management of GaN HEMT devices using serpentine minichannel heat sinks

Ahmed F. Al-Neama [a, b, *], Nikil Kapur [a], Jonathan Summers [a], Harvey M. Thompson [a]

[a] Institute of Thermofluids, School of Mechanical Engineering, University of Leeds, LS2 9JT, United Kingdom.

[b] Department of Mechanical Engineering, Faculty of Engineering, University of Mosul, Iraq.

*Corresponding author. Email: ahmedfalneama@gmail.com

Abstract:

An experimental and numerical investigation of water-cooled serpentine rectangular minichannel heat sinks (MCHS) has been performed to assess their suitability for the thermal management of gallium nitride (GaN) high-electron-mobility transistors (HEMTs) devices. A Finite Element-based conjugate heat transfer model is developed, validated experimentally and used to determine the optimal minichannel width and number of minichannels for a case with a uniform heat flux of 100 W/cm^2. The optimisation process uses a 30 point Optimal Latin Hypercubes Design of Experiments, generated from a permutation genetic algorithm, and accurate metamodels built using a Moving Least Square approach. A Pareto front is then constructed to enable the compromises available between designs with a low pressure drop and those with low thermal resistance to be explored and an appropriate minichannel width and number of minichannels to be chosen. These parameters are then used within conjugate heat transfer models of a serpentine MCHS with silicon, silicon carbide, diamond and graphene heat spreaders placed above a GaN HEMT heating source of area 4.8 × 0.8 mm^2, generating 1823 W/cm^2. A nanocrystalline diamond (NCD) layer with thickness of 2 µm is mounted on the top surface of the GaN HEMT to function as a heat spreader to mitigate the hot spots. The effect of volumetric flow rate and heat spreader thickness on the chip temperature has been investigated numerically and each of these has been shown to be influential. For example, at a volumetric flow rate of 0.10 l/min, the maximum chip temperature can be reduced from 124.7 ^{o}C to 96.7 ^{o}C by employing a 25 µm thick graphene heat spreader attached to the serpentine MCHS together with a NCD layer compared with a serpentine MCHS without these heat spreaders.

Keywords: Serpentine minichannel heat sink, Conjugate Heat Transfer, CFD, GaN HEMTs, Heat spreader, Multi-objective genetic algorithm, Nanocrystalline diamond layer.

Nomenclature

A_{base}	Base area of minichannel [m^2]	$T_{w,avg}$	Average channel base temperature [^{o}C]
A_{ch}	Cross-sectional area of minichannel [m^2]	$T_{w,tci}$	Channel base temperature at thermocouple location (i = 1–4), [^{o}C]
A_{eff}	Effective heat transfer area per channel [m^2]	V_{ch}	Velocity in microchannel [m/s]
A_{fin}	Surface area of fin [m^2]	W_w	Fin width [m]
A_h	Bottom heated area of the MCHS [m^2]	W_{ch}	Minichannel width [m]
Cp_f	Specific heat of fluid [J/kg.K]	W	Heat sink width [m]
D_h	Hydraulic diameter [m]		
h	Convective heat transfer coefficient [W/m^2.K]	**Greek symbols**	
H_b	Substrate thickness [m]		
H_{ch}	Minichannel height [m]	η_f	Fin efficiency
k	Turbulent kinetic energy [m^2/s^2]	ρ_f	Fluid density [kg/m^3]
k_f	Thermal conductivity of fluid [W/m.K]	μ_f	Dynamic viscosity of fluid [kg/m s]
k_s	Thermal conductivity of copper block [W/m.K]	μ_T	Turbulent viscosity [kg/m s]
k_T	Turbulent thermal conductivity [W/m.K]	ε	Channel surface roughness [μm]
L	Heat sink Length [m]	ω	Specific dissipation rate [1/sec]
L_{ch}	Minichannel length [m]		
n	Number of minichannel	**Subscripts**	
ΔP	Total pressure drop [Pa]	avg	Average
Q_{in}	Volumetric flow rate [m^3/sec]	f	Fluid (Water)
q	Heat transfer rate [W]	in	Inlet
Re	Reynolds number	out	Outlet
R_{th}	Total thermal resistance [K/W]	max	Maximum
$T_{f,avg}$	Fluid bulk temperature [^{o}C]	s	Solid
$T_{f,in}$	Inlet fluid temperature [^{o}C]	tci	Location of the thermocouple along the flow channel
$T_{f,out}$	Outlet fluid temperature [^{o}C]	Γ	Interface between the fluid and solid

1. Introduction

Over the last decade, gallium nitride (GaN) high-electron-mobility transistors (HEMTs) have become increasingly popular for radio-frequency (RF) and microwave applications due to their robustness, wide band-gap and high thermal conductivities and saturated electron velocities that enable them to function in harsh environments [1,2]. However, GaN HEMTs dissipate large heat fluxes which create hotspots that can cause significant degradation in performance [3] when maximum operating temperatures of ~250 ^{o}C are exceeded. To alleviate the problem of hotspots, silicon carbide (SiC) heat spreaders have been used due to their high thermal conductivity of 370 W/m.K at 20 ^{o}C [4]. However, since the thermal conductivity of SiC decreases significantly as temperature increases [5], the use of SiC alone is not practical for hot spot mitigation. For high heat fluxes (> 100 W/cm^2) single-phase liquid cooling and flow boiling in microfluidic systems can provide the required cooling [6]. The former, first introduced by Tuckerman and Pease [7] in 1981, have emerged as viable cooling devices for high heat flux electronics due to their high surface area to volume ratio [8]. The latter have also been widely studied by researchers due to their ability to dissipate high heat fluxes with much lower pumping power than the former due to their effective utilization of the latent heat of vaporization [9]. However, at higher heat fluxes, microchannel flow boiling suffers from pressure fluctuations and flow instabilities which can lead to serious problems from significant reductions in heat transfer performance due to, for example, liquid dry-out [6].

A number of investigations into the thermal management of GaN HEMTs have appeared in the literature. For example, Calame et al. [10] used experiments and numerical simulations to study the dissipation of 4 kW/cm^2 over a 1.2 × 5 mm^2 active area of a GaN on SiC semiconductor using water-cooled microchannel coolers, while the experimental study of Lee et al. [11] investigated how to dissipate a heat flux of 11.9 kW/cm^2 over eight heat sources of size 350 × 150 µm^2 on a 7 × 7 mm^2 silicon (Si) die with a maximum hotspot temperature of 175°C. Recently, Lee et al. [12,13] used 3-D numerical simulations to analyse the thermal conditions when a total power of 92.4 W is applied to 40 multiple gates (a heat flux of 330 kW/cm^2 is applied to each gate) located on GaN HEMTs on a SiC-based microchannel heat sink using water and methanol as a coolants in single and two phase flow conditions. Other relevant studies have focused on the effect of using very high thermal conductivity substrates to enhance heat spreading for GaN and a number of these have analysed diamond heat spreaders [14 – 16] since diamond's thermal conductivity is 2200 W/m.K – 5.5 times greater than copper [17]. Han et al. [18] used experiments and numerical simulations to investigate the effect of 300 µm thick diamond heat spreaders on copper-based microchannel heat sinks containing twenty–one parallel straight rectangular microchannels with a water flow rate of 0.4 l/min to dissipate 11.9 kW/cm^2 from a GaN-on-Si device. They found that the use of the diamond heat spreader within the liquid-cooled microchannel heat sink enabled, the maximum gate finger temperature to be reduced from 237 ^{o}C to 193 ^{o}C compared with a heat sink without a heat spreader.

Graphene, on the other hand, may be a viable alternative to diamond not only because it is less expensive, but also because of its extremely high thermal conductivity which ranges from 3080 – 5300 W/m·K at room temperature [19, 20]. In addition, its low density and strength (50-times stronger than steel [21]) has created excitement within research teams worldwide. The effect of graphene heat spreaders on operating temperatures have been investigated numerically by Barua et al. [22], Bae et al. [23] and Subrina et al. [24], while Reddy and Dulikravich [25] used a three-dimensional conjugate heat transfer model to investigate the effect of the single- and few-layer graphene nano-platelet heat spreaders applied to the top wall of micro pin-fin heat sinks on the maximum electronic chip temperature. The latter's results showed that the use of such thin graphene nano-platelet heat spreaders can lead to significant reductions in the maximum chip temperature.

However, research has shown that heat spreaders by themselves are insufficient for high heat flux applications and that nanocrystalline diamond (NCD) around the gates can be extremely beneficial under these condition. In recent years, NCD thin-films have advanced significantly [26] due to their unique properties, notably high thermal conductivity (up to 1300 W/m.K for $t_{NCD} > 3$ µm) [27]. To mitigate the self-heating effect, NCD has been demonstrated as a top-side coating for improved heat spreading in AlGaN/GaN HEMT devices by Anderson et al. [28]. As a result, HEMTs with NCD heat spreading layers exhibit a 20% decrease in peak channel temperature compared to HEMTs without an NCD film. Tadjer et al. [29,30] also used a Nanocrystalline diamond heat-spreading film with thickness of 0.5 µm mounted on the top surface of the AlGaN/GaN HEMT device in order to reduce self-heating. Their results showed significant reduction in temperature near the GaN/Si substrate interface, from 340 ^{o}C to 120 ^{o}C after NCD capping.

The vast majority of previous studies have used straight rectangular microchannel heat sinks with heat spreaders to dissipate high heat flux from the GaN HEMTs. Since the boundary layer thickness increases along the flow direction in these straight channels, they suffer from a continuous increase of surface temperature along the flow direction and a deterioration in heat transfer performance. The use of serpentine channels has recently been shown to provide much better heat transfer performance, due to a combination of being able to disrupt fully-developed boundary layers through the curved channel ends and from the secondary flow structures (Dean vortices) which are generated in the serpentine bends and which also improve fluid mixing and heat transfer.

Al-Neama et al. [31] have very recently used complementary experimental and numerical methods to investigate the benefits of employing three different serpentine microchannel heat sink designs using single (SPSM), double (DPSM) and triple path serpentine configurations (TPSM). Their performance was compared with that of a design based on straight rectangular microchannels (SRMs) in terms of pressure drop (ΔP), average Nusselt number (Nu_{avg}) and total thermal resistance (R_{th}). Their experimental and numerical results showed that the serpentine channel bends are very influential in improving heat transfer by preventing the hydrodynamic and thermal boundary layers attaining a fully-developed state. The SPSM design provides the most effective heat transfer, followed by the DPSM and TPSM ones, both of which

out-performed the SRM heat sink, and that the SPSM heat sink produced a 35% enhancement in Nu_{avg} and a 19% reduction in R_{th} at a volumetric flow rate of 0.5 l/min compared to the conventional SRM heat sink. These improvements in the heat transfer are, however, achieved at the expense of significantly larger ΔP. Another experimental and numerical study have been conducted by Al-Neama et al. [32] where the SPSM heat sink was modified by integrating a small chevron fins between the main channel flow to generate secondary flow to enhance fluid mixing as well as convective heat transfer. This novel design is found to significantly reduce both the pressure drop across the heat exchanger and the total thermal resistance by up to 60% and 10%, respectively, and to enhance the average Nusselt number by 15%.

The present study is the first to consider the feasibility and performance of using serpentine, rather than conventional straight, water-cooled channel heat sinks for dissipating the high heat fluxes associated with GaN HEMTs. It further extends the recent work of Al-Neama et al. [31] to explore and demonstrate the significant additional benefits of using a range of different heat spreader materials, on the cooling of CREE CGHV1J070D GaN HEMT dies [33]. The paper is organised as follows: The MCHSs of interest, experimental apparatus and analytical techniques used to determine their temperature distribution and flow characteristics are described in section 2. The conjugate heat transfer models of the heat sink, heat spreader and GaN HEMT heating source are described in section 3 and a comprehensive series of experimental and numerical results is presented in section 4. Conclusions are drawn in section 5.

2. Experimental Methodology

2.1. Experimental set-up and procedure

A schematic diagram of the main components of the experimental test rig is depicted in Fig. 1. Water from a ~23 litre reservoir is pumped through the flow loop using a miniature diaphragm water pump. The flow rate is controlled by adjusting the pump speed by regulating the voltage from a DC-power supply and using a bypass flow loop and control valve to give a flow rate in the range 0.1 – 1.0 l/min, as measured on a flow meter (PLATON NG glass model). Clear plastic tubes with an outer/inner diameter of 4 mm/2.2 mm and fittings were used to construct the flow loop.

To measure the water temperature at the minichannel inlet and outlet simultaneously, K-type sheathed thermocouples with 0.5 mm probe diameter were used by inserting one at the water inlet point to the MCHS

and a second just after the water outlet from the MCHS. The water inlet temperature was 20 ºC throughout the experiments. To measure the total pressure drop between the inlet and outlet of the MCHSs, a digital pressure meter was used (model Comark C9555) having a range of 0 to 2.1 bar. Two power film resistors of resistance 10 Ω (MP9100 (TO-247)) were used as a heat source, and each one has cross-sectional area of 11.5 mm × 14 mm with the maximum power reaching 100 W (62 W/cm^2). These are mounted at the bottom of the MCHS. The voltage and current input to the power film resistor heater were controlled by a DC power supply unit with an output range of 0-35 V and 0-4 A. To minimise heat loss to the surrounding environment, the MCHS copper block was packed inside a bed of insulating fibre glass, and secured within a clear Acrylic Perspex plastic box of size (10×10×10) cm^3 with a cover.

2.2. Design and fabrication of the MCHS test sections

Serpentine minichannel heat sink test sections were designed using SolidWorks [34] then fabricated from copper (thermal conductivity of 388 W/m.K at 20 °C), using a high-accuracy Computer Numerical Control (CNC) milling machine (FANUC ROBODRIL). The parametric design of the serpentine MCHS model such as minichannel depth (H_{ch}), minichannel width (W_{ch}), fin width (W_w), footprint area ($W \times L$), heat sink depth (H) and substrate thickness (H_b) are kept at 2 mm, 1.5 mm, 1.0 mm, 38 mm × 38 mm, 4 mm and 2 mm, respectively, to give 12 parallel rectangular minichannels. Fig. 2(a) shows the isometric actual view and top view of the MCHS considered here.

Around the top of the heat sinks there is a groove made for an O-ring seal with a depth and width of 0.7 mm and 1.0 mm, respectively, to prevent water leakage. Each MCHS is assembled with an acrylic plastic sheet cover which is held onto the copper block by four stainless steel mounting screws (M3 × 0.5) and sealed with an O-ring. Two 3.0 mm holes with depth of 3.0 mm were drilled on the top side surfaces of the plastic covers and a male run tee union adapters (M3 × 0.5) are fixed into these threaded holes to provide the inlet and outlet for the water, and also allow access to measure the water temperature at the inlet and outlet. To measure the pressure drop between the inlet and outlet, a further two 3.0 mm holes of depth 3.0 mm were drilled into the sides of the plastic cover (to match the inlet and outlet positions), with barb fitting adapters (M3 × 0.5) used to connect the pressure gauge, see Fig. 2(b).

Two power film resistors were attached to the bottom of the MCHS test section using a thin layer of thermal Ethoxy (Electrolube, TCER) with thermal conductivity of 2.2 W/m.K. The thickness of the thermal Ethoxy layer is measured manually using a digital Vernier caliper, and was found to be 200 ± 7 µm. To record the junction (maximum) temperature of the resistor as accurately as possible, the procedure described in Ref. [31] was adopted. To measure the wall temperature distribution along the MCHS sample, four K-type sheathed thermocouples with 0.5 mm probe diameter were inserted in the copper block at a distance of 1mm below the minichannel base until it reaches half the width of the MCHS specimen. The locations of the thermocouple holes, as measured from the inlet of the MCHS and along its length are shown in Fig. 2(b). Thermal paste was used to fill the holes to ensure accurate temperature measurement.

Sa and **Sq** which are respectively the Average Roughness and Root Mean Square Roughness are measured for both MCHS models using the BRUKER-NPFLEX-LA 3D Surface Metrology System, and these were found to be respectively 1 ± 0.1 µm and 1.2 ± 0.1 µm for each MCHS model. In the experiments, the relative surface roughness, ε/D_h, where ε and D_h are respectively the surface roughness and hydraulic diameter of the minichannel, is therefore 0.583×10^{-3}. This is less than the relative surface roughness of stainless steel micro-tubes (1.76×10^{-3} to 2.80×10^{-3}) in the study of Kandlikar et al. [35] who showed this ε/D_h had negligible effect on pressure drop and heat transfer characteristics; consequently the effect of the surface roughness (ε) on the pressure drop and heat transfer coefficient is neglected in the present study.

2.3. Experimental measurements and data analysis

2.3.1. Heat transfer analysis

Before conducting any experiments, the rate of heat loss from the MCHS specimen to the surroundings was first determined. In the present work, the procedure described in Ref. [31] has been used, and the maximum average heat loss was found to be approximately 6% of the input power to the model.

The average heat transfer coefficient (h_{avg}) can be calculated from Newton's law of cooling as:

$$h_{avg} = \frac{q}{A_{eff}\left(T_{w,avg} - T_{f,avg}\right)} \tag{1}$$

where q is the total heat supplied into the MCHS. The average fluid temperature can be calculated as ($T_{f,avg} = \left(T_{f,in} + T_{f,out}\right)/2$), where $T_{f,in}$ and $T_{f,out}$ are respectively the fluid inlet and outlet temperatures

which are measured by the thermocouples positioned just before and after the heat sink test section. The average minichannel base temperature can be obtained by:

$$T_{w,avg} = \frac{\sum_{i=1}^{4} T_{w,tci}}{4} \tag{2}$$

Since direct measurement of the channel base temperature is challenging, it is determined by assuming one-dimensional steady state heat conduction between the thermocouple location (tci) and the minichannel base in the y direction, the local minichannel base temperature ($T_{w,tci}$) can be evaluated by [36]:

$$T_{w,tci} = T_{y,tci} - \frac{y \,.\, q}{A_h \cdot k_s} \tag{3}$$

$T_{y,tci}$ represents the temperature close to the minichannel base wall which was measured experimentally using a thermocouple, the subscript i denotes the location of thermocouple used to measure the minichannel base temperature. A_h denotes the area of the substrate subjected to heat flux, while k_s is the thermal conductivity of the heat sink material, and y is the distance between the bottom wall of the minichannel and the thermocouple that is embedded to measure $T_{y.tci}$ as shown in Fig. 2(b). In the present work, the heat is transferred to the fluid through three minichannel walls only and the fourth (Top) wall is assumed to be adiabatic. Hence, A_{eff} which represents the surface area available for heat transfer and can be calculated as:

$$A_{eff} = A_{base} + \eta_f \cdot A_{fin} \tag{4}$$

The term η_f is defined as the fin efficiency assuming an adiabatic tip condition which is correlated by:

$$\eta_f = \frac{tanh(m \cdot H_{ch})}{m \cdot H_{ch}} \qquad \text{where the fin parameter } (m) \text{is given by} \qquad m = \sqrt{\frac{2h_{avg}}{W_w \cdot k_s}} \tag{5}$$

while A_{base} and A_{fin} represent the minichannel base and fin area available for heat transfer, respectively. A_{base} can be calculated as:

$$A_{base} = nW_{ch} \cdot L_{ch} + \frac{\pi}{2}(n-1)(r_1^2 - r_2^2) + 2W_{ch}\left(L - \left(W_{s1} + W_{s2} + r_1 + L_{ch} + \frac{W_{ch}}{2}\right)\right) + \pi\left(\frac{W_{ch}}{2}\right)^2 \tag{6}$$

where L_{ch} represents the length of the straight minichannel, $L_{ch} = L - (2r_1 + W_{s1} + W_{s2})$, and W_{s1} and W_{s2} are the outside wall thicknesses, see Fig. 2(a). The symbols r_1 and r_2 denote the outer and inner radius

of the curved minichannel respectively, whereas n represents the number of minichannels. A_{fin} can be determined by:

$$A_{fin} = 2nH_{ch} \cdot L_{ch} + \pi H_{ch}(n-1)(r_1 + r_2) + 4H_{ch}\left(L - \left(W_{s1} + W_{s2} + r_1 + L_{ch} + \frac{W_{ch}}{2}\right)\right) + \pi W_{ch} \cdot H_{ch} \quad (7)$$

The corresponding average Nusselt number can be determined by:

$$Nu_{avg} = \frac{h_{avg} \cdot D_h}{k_f} \quad (8)$$

where k_f represents the water's thermal conductivity evaluated at the average fluid temperature ($T_{f,avg}$). D_h denotes the minichannel hydraulic diameter $\left(D_h = \frac{4A_{ch}}{P_w} = \frac{2\,(W_{ch} \cdot H_{ch})}{W_{ch} + H_{ch}}\right)$, while P_w and A_{ch} are respectively the wetted perimeter and the cross-sectional area of the minichannel.

2.3.2. Total thermal resistance

The total thermal resistance (R_{th}) of the serpentine MCHS can be determined as follows:

$$R_{th} = \frac{T_{surf,max} - T_{f,in}}{q} \quad (9)$$

where $T_{surf,max}$ is the maximum surface temperature of the heat sink. The total thermal resistance of the heat sink comprises three main components which are conductive (R_{cond}), convective (R_{conv}) and bulk temperature-rise (R_{bulk}) thermal resistances [37], and can be expressed by:

$$R_{th} = R_{cond} + R_{conv} + R_{bulk} = \frac{H_b}{k_s \cdot A_h} + \frac{1}{h_{avg} \cdot A_{eff}} + \frac{1}{\dot{m} \cdot C_{p_f}} \quad (10)$$

where $\dot{m}$ is the total mass flow rate of coolant through microchannel ($\dot{m} = \rho_f \cdot V_{ch} \cdot A_{ch}$). The C_{p_f} denotes the specific heat capacity of the fluid which is evaluated at the $T_{f,avg}$. In this study, the conductive thermal resistance remains constant since the substrate thickness of the heat sink is unchanged. While convective and bulk thermal resistances reduce with increasing water flow rate, resulting in lower total thermal resistance. The R_{bulk} is caused by the heating of the fluid as it flows through the minichannels and absorbs heat [37].

2.3.3. Pressure drop analysis

A digital pressure gauge was used to measure the total pressure drop (ΔP) directly using two plastic tubes connected to the barb fitting adapters, see Fig. 2(b). The serpentine MCHS structure has n minichannels and a total $n-1$ fins (U-bends), see Fig. 2(a), and the total pressure drop is caused by contributions from friction in the straight minichannels and from the U-bends. The procedures used to calculate ΔP are described in detail in Ref. [31].

2.4. Experimental uncertainty

The ASME standard [38] and the Root-Sum-Square (RSS) method described by Coleman and Steele [39] were used to estimate the experimental uncertainties. In the experiments, an electronic digital Vernier caliper is used to measure various geometric dimensions of the MCHS test sections. Uncertainties for various critical parameters are tabulated in Table 1.

3. Conjugate heat transfer model

3.1. Boundary conditions

The computational domain and boundary conditions are shown in Fig. 3. No-Slip and wall temperature boundary condition $\mathbf{u_s} = 0$ and $T_s = T_{f\ at\ wall}$ are used at solid walls. At liquid-solid boundaries the conductive and convective heat transfer to the fluid are coupled by imposing heat flux continuity at the interface between the fluid and the solid walls [40] as shown in Fig. 3(a), where $T_{s,\Gamma}$ and $T_{f,\Gamma}$ are respectively the interface temperature for the solid and the liquid. The boundary conditions of inlet flow are Q_{in} (m^3/s) and $T_{f,in}$ = 20 °C while the outlet flow boundary condition is $p = p_o$, where p_o is the pressure at the outlet (0 Pa), as shown in Fig. 3(b).

Except at the bottom of the MCHS, all the outer surface boundaries are considered to be adiabatic. Heating power, q, was applied at the bottom surface of the MCHS using $(-\boldsymbol{n}.(-k_s \nabla T) = q/A_h)$, where $\boldsymbol{n}$ denotes the outward normal vector on the boundary of the domain. Two power film resistors of resistance 10 Ω were used as heat sources, each with an effective heating area of 11.5 × 14 mm^2, and a heat flux of 62 W/cm^2. To define the thickness and thermal conductivity of the material (Ethoxy) located between the heater and the base of the heat sink, a thin layer boundary condition was employed, as shown in Fig. 3(c).

The thermal conductivity (k_l) and thickness (d_l) of the Ethoxy layer are respectively 2.2 W/(m.K) and 200 µm.

The thermo-physical properties of water including ρ_f, μ_f, C_{p_f} and k_f depend on temperature as shown in Eqs. (11-14) [41]:

$$\rho_f = 838.466 + 1.40T - 0.0030T^2 + 3.72 \times 10^{-7}T^3 \quad (11)$$

$$\mu_f = 1.38 - 0.0212T + 1.36 \times 10^{-4}T^2 - 4.646 \times 10^{-7}T^3 + 8.90 \times 10^{-10}T^4 - 9.08 \times 10^{-13}T^5 + 3.846 \times 10^{-16}T^6 \quad (12)$$

$$C_{p_f} = 12010.147 - 80.407T + 0.3099T^2 - 5.382 \times 10^{-4}T^3 + 3.625 \times 10^{-7}T^4 \quad (13)$$

$$k_f = -0.869 + 0.00895T - 1.584 \times 10^{-5}T^2 + 7.975 \times 10^{-9}T^3 \quad (14)$$

where the temperature T is in K. The thermal conductivity of copper k_s= 400 W/m.K in all computations.

3.2. Governing equations

A numerical model of the three-dimensional flow and heat transfer in the MCHS was developed under the assumptions that: (1) the flow and heat transfer are steady; (2) flow is incompressible and single-phase in both the laminar and turbulent flow regimes; (3) the effects of radiation and buoyancy are negligible. The Reynolds number (Re) can be calculated as:

$$Re = \frac{\rho_f \cdot V_{tube} \cdot D_h}{\mu_f} \quad (15)$$

where ρ_f and μ_f are respectively the density and viscosity of the fluid, while V_{tube} denotes the inlet velocity to the tube having hydraulic diameter (D_h) of 1.5 mm for both MCHS models, see Fig. 2(b). When $Re \leq 2300$ flow is considered laminar, and turbulent with $Re > 2300$. Flow is modelled using the following incompressible, steady continuity and Navier-Stokes momentum equations:

$$\nabla \cdot \mathbf{u} = 0 \quad \text{(continuity equation)} \quad (16)$$

$$\rho_f(\mathbf{u} \cdot \nabla)\mathbf{u} = \nabla \cdot \left[-p\mathbf{I} + \mu_f(\nabla\mathbf{u} + (\nabla\mathbf{u})^T)\right] \quad \text{(momentum equation for laminar flow)} \quad (17)$$

$$\rho_f(\mathbf{u} \cdot \nabla)\mathbf{u} = \nabla \cdot \left[-p\mathbf{I} + (\mu_f + \mu_T)(\nabla\mathbf{u} + (\nabla\mathbf{u})^T)\right] \quad \text{(momentum equation for turbulent flow)} \quad (18)$$

where $\mathbf{u}$ and p are respectively the fluid velocity vector and the fluid pressure (Pa), and $\mathbf{I}$ denotes the unit matrix. The standard k-ω turbulence model has been used to solve the governing equations, as this model has been shown to capture the physics well for other similar heat transfer studies [31, 42, 43]. The k-ω model introduces two additional variables: the turbulent kinetic energy, k (m^2/s^2), and specific dissipation

rate, ω $(1/s)$. The transport equations for k and ω used in the CFD model are based on those given by Wilcox [44]:

$$\rho_f(\mathbf{u}\cdot\nabla)k = \nabla\cdot\left[\left(\mu_f + \mu_T\sigma_k^*\right)\nabla k\right] + P_k - \rho_f\beta_o^*\omega k \tag{19}$$

$$\rho_f(\mathbf{u}\cdot\nabla)\omega = \nabla\cdot\left[\left(\mu_f + \mu_T\sigma_\omega\right)\nabla\omega\right] + \alpha\frac{\omega}{k}P_k - \rho_f\beta_o\omega^2 \tag{20}$$

The production term and the turbulent viscosity are defined by:

$$P_k = \mu_T[\nabla\mathbf{u}:(\nabla\mathbf{u} + (\nabla\mathbf{u})^T)]\,, \qquad \mu_T = \rho_f\frac{k}{\omega} \tag{21}$$

while the empirical turbulent model constant parameters are [31]:

$$\alpha = \frac{13}{25}, \qquad \sigma_k^* = \frac{1}{2}, \qquad \sigma_\omega = \frac{1}{2}, \qquad \beta_o = \frac{9}{125}, \qquad \beta_o^* = \frac{9}{100}$$

The heat transfer (energy) equations for the liquid and the solid can be expressed respectively as:

$$\rho_f C_{p_f}\mathbf{u}\cdot\nabla T = \nabla\cdot\left(\left(k_f + k_T\right)\nabla T\right) \tag{22}$$

$$\nabla\cdot(k_s\nabla T) = 0 \tag{23}$$

where C_{p_f} denotes the specific heat capacity of the fluid which is evaluated at the average fluid temperature, while k_T is the turbulent thermal conductivity $\left(k_T = \frac{\mu_T.C_{p_f}}{Pr_T}\right)$, and Pr_T is the turbulent Prandtl number (following Kays- Crawford [45]). Eq. (22) is the energy equation for the liquid in three-dimensional, steady and turbulent flow, with $\mu_T = 0$ for laminar flow. The above flow and heat transfer equations are solved within COMSOL Multiphysics version 5.2 [41].

4. Results and discussion

4.1. Effect of grid density

The effect of grid density on the numerical solutions is investigated using a range of mesh sizes. The heat sink and serpentine minichannel dimensions used in these simulations are similar to those used in the experimental set-up, see Fig. 2(a). Two heat sources are used to simulate the experimental work and each one has cross-sectional area of 11.5 mm × 14 mm and height of 1.0 mm (see Fig. 3(c)). These are mounted underneath the MCHS and supply 100 W in total (62 W/cm^2).

The effect of grid density on the predicted value of the temperature between the heater and the bottom of the heat sink ($T_{junction}$) and total pressure drop (ΔP) is given in Table 2, where grid 1 is the coarsest and

grid 4 is the finest. These results were generated at a water flow rate of $106\ ml/min$ (U_{in} = 1 m/s), with the water inlet temperature set at 20 °C. The percentage differences between solutions, E, are calculated with respect to the solutions on grid 4 in each case. The solutions after grid 3 are effectively grid independent and all numerical solutions reported below have been obtained using grid 3.

4.2. Model validation

The numerical model was validated against the present experimental work for serpentine MCHSs in terms of total thermal resistance (R_{th}), total pressure drop (ΔP) and average Nusselt number (Nu_{avg}). Fig. 4(a) compares the experiments against corresponding numerical predictions of R_{th} and ΔP for a serpentine MCHS with volumetric flow rates (Q_{in}) ranging from 0.053 to 0.318 l/min, which corresponds to Reynolds number of 747–4482, and a heat flux of 62 W/cm^2. Good agreement between experimental data and corresponding numerical predictions was obtained, with an average discrepancies of 7.8% for ΔP and 3.2% for R_{th}.

Generally, it is seen that ΔP increases and R_{th} decreases as the Re increases. The latter is due to decreases in both R_{conv} and R_{bulk} as Re increases since R_{cond} remains constant since the heat sink base thickness is fixed at 2 mm. The reduction in R_{conv} is due to the higher heat transfer coefficient while the reduction in R_{bulk} is due to the higher flow rate, see Eq. (10). The minichannel bends at the end of each minichannels are very influential since they prevent the hydrodynamic and thermal boundary layers from attaining a fully-developed state, albeit with a significantly increased pressure drop.

Fig. 4(b) compares the average Nusselt numbers (Nu_{avg}) and the average channel base temperatures ($T_{w,avg}$) obtained experimentally and computationally for the serpentine MCHS as a function of Reynolds number ranging from 747 to 2988 ($0.053 \leq Q_{in} \leq 0.212\ l/min$) with a heat flux of 62 W/cm^2. To calculate the Nu_{avg} values, Eq. (8) was used while Eq. (1) was used to determine the average heat transfer coefficient (h_{avg}). Generally, Nu_{avg} increases with Re as the thermal boundary layer thickness decreases with the increased fluid velocity [46]. The numerical predictions are in good agreement with the experiments, with an average discrepancy of 3.2%. $T_{w,avg}$ was estimated from the values at the four thermocouples closest to the minichannel base (see Eq. (2) and Fig. 2(b)). $T_{w,avg}$ decreases with Re due to the effects of thermal

boundary layer re-development and good mixing in the minichannel bends. Once again, good agreement was found between experimental and computational data with an average discrepancy of 2.4%.

4.3. Serpentine MCHS design optimisation

Heat sinks must be designed according to the conflicting requirements of minimising thermal resistance (R_{th}) and minimising pressure drop (ΔP). Here, the goal is to carry out the multi-objective optimisation of minimising R_{th} and ΔP for serpentine MCHSs by accounting for two important design variables, namely the minichannel width (W_{ch}) and the number of minichannel (N_{ch}) in the ranges of $0.5\ mm \leq W_{ch} \leq 1.0\ mm$ and $5 \leq N_{ch} \leq 10$. The optimisation was carried out at constant volumetric flow rate of $Q_{in} = 0.10\ l/min$ with an inlet water temperature to the MCHS set to 20 °C, and constant heat flux of 100 W/cm^2 supplied underneath the heat sink. The area ($W \times L$), substrate thickness (H_b) and minichannels depth (H_{ch}) of the heat sink are constant and are respectively 10 mm × 10 mm, 0.5 mm and 1.5 mm. The goal is to construct a Pareto front of non-dominated solutions, from which an appropriate compromise design can be chosen.

The Pareto front is obtained by building accurate metamodels of both ΔP and R_{th}, as a function of the two design variables. The metamodels are constructed using the R_{th} and ΔP values extracted from numerical simulations carried out at 30 Design of Experiment (DoE) points obtained using Optimal Latin Hypercubes (OLHCs), via a permutation genetic algorithm using the Audze-Eglais potential energy criterion to create an efficient distribution of DoE points [47]. The points are distributed as uniformly as possible when the potential energy of repulsive forces, which is inversely proportional to the squared distance between the points, is minimised [48]:

$$min\ E^{AE} = min \sum_{i=1}^{N} \sum_{j=i+1}^{N} \frac{1}{L_{i,j}^2} \tag{24}$$

where $L_{i,j}$ is the Euclidean distance between the points i and j ($i \neq j$) and N=30 is the number of DoE points. Metamodels for R_{th} and ΔP throughout the design space are built using a Moving Least Squares (MLS) method [49], with a second order (Quadratic) base polynomial, where a Gaussian weight decay function, w_i, is used to determine the weighting of points in the regression coefficients at each point, see Eq. (25).

$$w_i = e^{-\theta \cdot r_i^2} \quad (25)$$

The parameter r_i is the normalised distance of the metamodel prediction location from the i^{th} sampling point [47]. By adjusting the closeness of fit parameter, θ, the influence of numerical noise in the responses can be controlled. The Pareto front is calculated using a multi-objective genetic algorithm (MOGA) approach based on [50, 51]. Points on the Pareto front are non-dominated in the sense that it is not possible to decrease any of the objective functions (i.e. ΔP or R_{th}) without increasing the other objective function. Fig. 5 shows the values of the ΔP and R_{th} at all of the DoE points and the Pareto front that is constructed from them.

Fig. 5 shows seven points on the Pareto front ($P_1 - P_7$) and a comparison between the calculated values of ΔP and R_{th} from the metamodels at these points and from the full numerical simulations. Agreement between the metamodel and full numerical predictions is good in all cases with an average error of 1.8% for R_{th} and 4.2% for ΔP, demonstrating the accuracy of the metamodelling approach adopted here. Fig. 5 also shows the compromise that must be struck between pressure drop and thermal resistance. It shows, for example, that achieving the relatively low thermal resistance at P_1 (0.278 K/W) requires more than eight times the pressure drop than for the higher thermal resistance of 0.412 K/W at P_7. Clearly the most appropriate compromise depends on the particular manufacturing and operating cost and functionality requirements for a specific heat sink. The subsequent MCHSs used below for the cooling of GaN HEMTs will be based on the design parameters from the Pareto point P_5 in Fig. 5.

4.4. Cooling of GaN HEMTs using serpentine MCHSs

This section presents a numerical investigation into the capability of a water-cooled copper serpentine MCHS with a footprint of 10 mm × 10 mm and a thickness of 2.0 mm, based on the design parameters at Pareto point P_5 with 7 minichannels shown in Fig. 5, to dissipate heat generate from the GaN HEMT. The minichannel width (W_{ch}), fin width (W_w), and minichannel depth (H_{ch}) are kept at 0.75 mm, 0.594 mm, and 1.5 mm, respectively. The inlet water temperature is set at 20 ^{o}C. A heat spreader having the same base area as the serpentine MCHS with different thickness was attached directly at the bottom of the heat sink base, with 50 µm thick of 80Au/20Sn solder mounted between the heat spreader and the MCHS as a bounding material. The thermal conductivity of the solder is set to 57 W/m.K [18].

As a typical heat source, a CREE CGHV1J070D GaN HEMT die [33] is selected for study. Fig. 6(a) shows a schematic of the transistor layout showing multi-fingered configurations, where source (S), gate (G), and drain (D) metallizations are indicated. One GaN HEMTs is simulated, having an area of 4800 × 800 µm^2 and a thickness of 2 µm, and located at the centre of the MCHS. The transistor is composed of 72 gate fingers that are mounted on the top surface of the GaN transistor to dissipate a total power of 70 W. The length (l_G) and width (W_G) of each gate are respectively 0.25 µm and 250 µm. Almost all of the heat is generated under each gate finger [18].

Single-phase, laminar flow conjugate heat transfer simulations are performed for a whole serpentine MCHS using COMSOL Multiphysics v.5.2 and the same assumptions used in section 3.1. The computational domain and boundary conditions used are shown in Fig. 6(b). Except at the bottom of the MCHS, all the outer surface boundaries (other than the flow inlet and outlet) are considered to be adiabatic. The heat flux of 1823 W/cm^2 is applied to the 72 gate fingers resulting in a heat flux of 1.556 MW/cm^2 loaded on each gate finger, with a power density of 3.89 W/mm. The effect of four different heat spreader materials is investigated: silicon (Si), silicon carbide (SiC), diamond and graphene (few-layer graphene). The temperature-dependent thermal conductivity of the Si, SiC, the diamond heat spreaders and the GaN layers are taken from references [18, 52], while for the copper heat sink the thermal conductivity is assumed to be constant. Following [25], the thermal conductivity of the few-layer graphene heat spreaders, with thicknesses ranging from 5 µm to 25 µm, are taken to have the constant value of 2000 W/m.K. The thermal boundary resistance (TBR) between GaN and heat spreader is included, and the value is assumed to be 3.3×10^{-8} m^2.K/W for all heat spreaders used [18, 25, 53]. The thermal properties and thickness of each material used in the simulations are listed in Table 3.

A 50 nm silicon nitride (SiN) layer was mounted on the top surface of the GaN HEMT to serve as device passivation and a nucleation dielectric for diamond [28]. A 2 µm nanocrystalline diamond (NCD) layer was implemented on top of the SiN layer to mitigate the problem of self-heating of the GaN transistor (see Fig. 6(c)), the details of these two layers can be found in Table 3.

4.4.1. Effect of grid density

The effect of grid density on the numerical solution of the conjugate heat transfer problem with both serpentine and straight rectangular MCHSs, a diamond heat spreader, a GaN transistor and a NCD layer within a SiN as a passivation surface is explored using four different mesh sizes, as indicated in Table 4. In order to facilitate a fair performance comparison between the two different MCHS both heat sink models share the same design parameters, and the dimensions of the Pareto point P_5 is selected as the optimum design for the serpentine MCHS model.

A tetrahedral mesh is generated to discretize the domain, with increasing grid refinement in the region of the GaN HEMT and gate fingers where the local heat flux is very high, as shown in Fig. 6(d). The volumetric flow rate and inlet temperature of the water are set to be 0.10 l/min and 20 ^{o}C, respectively. The heat flux density applied for each gate finger was 1.556 MW/cm^2 (the total power supplied on the GaN HEMT is 70 W), and a 300 µm thick diamond heat spreader is used. As shown in Table 4, for the conventional straight rectangular MCHS, compared to the results of a grid 3 (~ 4.5 million elements), grid 2 showed a 3.1% change in the maximum chip temperature (T_{max}), whereas using grid 4 resulted in only a 0.9% change in T_{max}. Similar behaviour was found for the serpentine MCHS so that grid 3 was used in all subsequent numerical solutions.

From the comparison between both heat sink designs, the maximum temperature (T_{max}) for the serpentine MCHS with diamond heat spreader and NCD layer is 65.70 ^{o}C, compared to 72.66 ^{o}C for the conventional straight rectangular MCHS. This is due the influence of the minichannel bends in the serpentine MCHS which disrupt the hydrodynamic and thermal boundary layers and maintain a state of developing flow [31,32]. However, the differential pressure between the inlet and outlet of the serpentine channel is significantly higher than those from straight channel.

4.4.2. Validation against previous studies

The numerical solutions for the GaN HEMTs cases were validated against the experimental results of Han et al. [18], which used eight GaN resistors (each size 350 × 150 µm^2 with a heat flux between 2.38–11.9 kW/cm^2) with 10–50 W total power mounted on a diamond heat spreader to enhance the hotspot cooling capability of a single-phase water-cooled straight rectangular microchannel heat sink. The conjugate heat transfer problem for the entire straight rectangular microchannel heat sink, heat spreader and GaN HEMTs

system was solved numerically for comparison with Han et al. [18]. The water flow rate across the entire microchannel heat sink was fixed at 0.4 l/min, leading to a laminar flow regime. As illustrated in Fig. 7(a), good agreement was obtained between Han et al.'s experiments and the simulation results for maximum heater temperature (T_{max}), with an average discrepancy of around 4.2% for the cases with and without a diamond heat spreader. Fig. 7(b) compares the temperature distribution across all the transistors between those measured by Han et al. [18] and the current simulation at total power of 50 W for cases with and without diamond heat spreader. Again good agreement was obtained with an average discrepancy of around 5.3%.

4.4.3. Effect of heat spreader materials

The effect of heat spreader material, namely Si, SiC and diamond is investigated numerically with and without an NCD layer. The thickness of the heat spreaders ($t_{spreader}$) are fixed at 300 µm and a heat flux of 1823 W/cm^2 is dissipated from the GaN HEMT. Once again 7 minichannels of width 0.75 mm are used while the GaN transistor dimension are shown in Fig. 6(a). The effect of the heat spreader material, NCD layer and Q_{in} on T_{max} with a water inlet temperature of 20 ^{o}C under laminar flow conditions can be seen in Fig. 8. The T_{max} values decrease as flow rates increases for all cases studied and these decrease significantly when the diamond heat spreader is used, whereas the inclusion of the SiC and especially Si heat spreaders have a deleterious effect on T_{max} compared to the case when no heat spreader is used. This is due to the fact that the Si has much lower thermal conductivity than SiC, Cu and diamond, and that its thermal conductivity reduces further as the temperature increases.

Integrating a 2 µm thick NCD layer on the top surface of the GaN HEMT has a significant effect on T_{max} for all heat spreader materials used. For example, at Q_{in}= 0.10 l/min, T_{max} for the serpentine MCHS with both diamond heat spreader and NCD film is 65.70 ^{o}C, compared to 90.66 ^{o}C and 124.7 ^{o}C for the serpentine MCHS with just diamond heat spreader and the serpentine MCHS without both heat spreader and NCD layer, respectively.

Fig. 9 shows the effect of heat spreader material (Si, SiC and diamond) on the temperature distribution across 72 gate fingers mounted on the top surface of the GaN transistor and capped with a layer of NCD for the case with $Q_{in} = 0.10\ l/min$, $t_{spreader}$ = 300 µm and heat flux of 1823 W/cm^2, these were

compared with the serpentine MCHS without both heat spreader and NCD layer. As expected based on the above results, the maximum gate temperature was found for the GaN–on–Si heat spreader case, while that for the GaN–on–diamond heat spreader was the lowest. Note that the maximum gate finger temperature for all heat spreaders are lower than the critical operating condition temperature ~225 ^{o}C [33].

4.4.4. Effect of heat spreader thicknesses

The effect of heat spreader thickness is now investigated, using thicknesses ranging from 100 µm to 600 µm for cases with Q_{in}= 0.10 l/min and heat flux of 1823 W/cm^2. The numerical simulations are conducted for the serpentine MCHS with different heat spreader materials (Si, SiC and diamond) without using an NCD layer, to examine the effect of the heat spreader alone on the temperature of the GaN HEMT. Fig. 10 shows that increasing the heat spreader thickness has relatively modest benefits for diamond and SiC heat spreader thicknesses less than about 300 µm, after which increasing spreader thickness has no significant benefit. In all cases T_{max} increases progressively from diamond to SiC heat spreaders. In contrast, for the Si heat spreaders, the comparatively low thermal conductivity means that increasing spreader thickness is actually detrimental with T_{max} increasing from around 207 ^{o}C to 253 ^{o}C as spreader thickness increases from 100 µm to 600 µm.

4.4.5. Few-layer graphene heat spreaders

Graphene has demonstrated an extremely high intrinsic thermal conductivity, which is approximately 5300 W/m.K at room temperature [54] for a single atomic plane of graphene with an approximate thickness of 0.335 nm. For few-layer graphene (FLG), the thermal conductivity decreases drastically as the number of layers increases, and will soon approach bulk graphite limit (~2000 W/m.K) [22, 55]. Although the thermal conductivity of FLG has not been reported yet, it can be expected to be between the values measured for single-layer graphene and bulk graphite [19 ,24]. Since the properties of graphene are functions of its number of layers, it is important to know the number of graphene layers, and this can be calculated by dividing the measured graphene thickness on the single-layer graphene thickness (0.335 mm) [55].

Fig. 11 shows the simulated maximum temperature of the GaN HEMTs as a function of the thermal conductivity in the range 1000 to 5000 W/mK and thicknesses of the graphene heat spreader (5 µm $\leq$ $t_{spreader}$ $\leq$ 25 µm). For a 5 µm thick graphene heat spreader, the number of graphene layers is around

14925, while for a 25 µm thick spreader there are approximately 74626 graphene layers. Figure 11 shows that as the thermal conductivity and thickness of the heat spreader increase the peak temperature is alleviated due to an increasing heat flux directed away from the hot spots. This behaviour is consistent with the finding of Subrina et al. [24] through conducting a numerical simulation to address the thermal management of nano-electronic circuits. They observed that increasing of the graphene heat spreader thicknesses (layers) together with thermal conductivity leads to a decrease in the maximum temperature of a chip.

Fig. 12 shows the temperature distribution at the interface between the heat spreader and the GaN HEMT using serpentine MCHS with and without an NCD film for a heat flux of 1823 W/cm^2 and Q_{in} of 0.10 l/min. The ten gate fingers located in the middle of the GaN HEMT were used for comparison. Due to the sufficiently thick layers of graphene used in the present work, it can be assumed that the thermal conductivity of graphene recovers to values of high quality bulk graphite (2000 W/m.K), this approach was also adopted by Reddy and Dulikravich [25]. The maximum temperature at this interface for the heat sink with both the graphene heat spreader with thickness of 25 µm and NCD layer is 96.71 ^{o}C, while that of the heat sink with the graphene heat spreader alone is 123.5 ^{o}C, suggesting that using an NCD layer leads to much more effective mitigation of hot spots. The two cases have been compared with the serpentine MCHS has both the diamond heat spreader with thickness of 25 µm and NCD layer, and the maximum temperature was found to be 101.4 ^{o}C.

5. Conclusion

This paper has shown that water-cooled serpentine MCHSs can provide effective thermal management of the GaN HEMTs that are increasingly popular for radar frequency and microwave applications. It has also shown that the serpentine channels, which play a crucial role in disrupting thermal boundary layers to improve heat transfer, provide better heat transfer capability than conventional ones based on straight channels, albeit with a significantly larger pressure drop. The latter can, however, be reduced by careful optimisation of the MCHS geometry parameters and the multi-objective optimisation carried out here has demonstrated clearly the compromise that can be struck between maximum heat transfer and minimum pressure drop for serpentine MCHSs.

The role of heat spreaders and heat spreader materials has also been investigated and the numerical simulations have shown that from a list of graphene, diamond, SiC and Si, graphene is the most effective, followed by diamond at reducing both peak chip temperature and peak heat flux over hot spots. However the temperature-dependent conductivity of SiC and Si mean that these heat spreaders are detrimental and increase the maximum chip temperature compared to the case without a heat spreader. Further, the numerical results showed that increasing the heat spreader thickness yields modest benefits for diamond and SiC heat spreaders with thicknesses less than about 300 µm, after which increasing spreader thickness has no significant benefit. In contrast, for Si heat spreaders the comparatively low thermal conductivity means that increasing spreader thickness is detrimental and leads to an increase in the maximum chip temperature from 207 ºC to 253 as the spreader thickness is increased from 100 µm to 600 µm. These results provide useful information for the optimisation of the thermal design of heat sinks for GaN HEMTs. Using an NCD thin layer has also a significantly beneficial effect, where its ability to dissipate high heat flux from a GaN HEMT leads to a significant reduction of the chip temperature and improved mitigation of hot spots.

Acknowledgements

The authors would like to express their deepest gratitude for the Iraqi Ministry of Higher Education and Scientific Research (MOHE) and Mechanical Engineering Department University of Mosul, Iraq, to provide financial support for this research project.

References:

[1] C.-W. Tsou, C.-Y. Lin, Y.-W. Lian, S.S.H. Hsu, 101-GHz InAlN/GaN HEMTs on Silicon with high Johnson's Figure-of-Merit, IEEE Transactions on Electron Devices, 62(8) (2015) 2675-2678.

[2] J. Millan, P. Godignon, X.Perpina, A. Perez-Tomas, J. Rebollo, A survey of wide bandgap power semiconductor devices, IEEE Transactions on Power Electronics, 29(5) (2014) 2155-2163.

[3] G. Agarwal, T. Kazior, T. Kenny, D. Weinstein, Modeling and Analysis for Thermal Management in Gallium Nitride HEMTs Using Microfluidic Cooling, ASME Journal of Electronic Packaging, In Press, October 2016, doi:10.1115/1.4035064.

[4] H. Lee, D.D. Agonafer, Y. Won, F. Houshmand, C. Gorle, M. Asheghi, K.E. Goodson, Thermal Modeling of Extreme Heat Flux Microchannel Coolers for GaN-on-SiC Semiconductor Devices, ASME Journal of Electronic Packaging, In Press, March 2016, 010907-1.

[5] K.M. Dowling, A.J. Suria, Y. Won, A. Shankar, H. Lee, M. Asheghi, K.E. Goodson, D.G. Senesky, Inductive Coupled Plasma Etching of High Aspect Ratio Silicon Carbide Microchannels for Localized Cooling, 2015, ASME Paper No. IPACK2015-48409.

[6] S.G. Kandlikar, W.K. Kuan, D.A. Willistein, J. Borrelli, Stabilization of flow boiling in microchannels using pressure drop elements and fabricated nucleation sites, Journal of heat transfer. ASME 128(4) (2006) 389-396.

[7] D.B. Tuckerman and R.F.W. Pease, High-Performance heat sinking for VLSI, IEEE Electron Device Letters EDL 2(5) (1981) 126-129.

[8] V. Yadav, K. Baghel, R. Kumar, S.T. Kadam, Numerical investigation of heat transfer in extended surface microchannels, International Journal of Heat and Mass Transfer 93 (2016) 612–622.

[9] T.G. Karayiannis, M.M. Mahmoud, Flow boiling in microchannels: Fundamentals and applications, Applied Thermal Engineering 115 (2017) 1372–1397.

[10] J.P. Calame, R.E. Myers, S.C. Binari, F.N. Wood, M. Garven, Experimental Investigation of Microchannel Coolers for the High Heat Flux Thermal Management of GaN-on-SiC Semiconductor Devices, International Journal of Heat and Mass Transfer, 50(23) (2007) 4767–4779.

[11] Y.J. Lee, B.L. Lau, Y.C. Leong, K.F. Choo, X. Zhang, P.K. Chan, GaN-on-Si hotspot thermal management using direct-die-attached microchannel heat sink, in Proc. IEEE 14th Electron. Packag. Technol. Conf., Singapore, (2012) 121–125.

[12] H. Lee, Y. Won, F. Houshmand, C. Gorle, M. Asheghi, K.E. Goodson, Computational Modeling of Extreme Heat Flux Microcooler for GaN-Based HEMT, 2015, ASME Paper No. IPACK2015-48670.

[13] H. Lee, D.D. Agonafer, Y. Won, F. Houshmand, C. Gorle, M. Asheghi, K.E. Goodson, Thermal Modeling of Extreme Heat Flux Microchannel Coolers for GaN-on-SiC Semiconductor Devices, 2016, ASME J. Electron. Packag, 138(1), p. 010907.

[14] J.G. Felbinger, M.V.S. Chandra, Y. Sun, L.F. Eastman, J. Wasserbauer, F. Faili, D. Babic, D. Francis, F. Ejeckam, Comparison of GaN HEMTs on Diamond and SiC Substrates, IEEE Electron Device Lett., 28(11) (2007) 948–950.

[15] D.I. Babić, Q. Diduck, P. Yenigalla, A. Schreiber, D. Francis, F. Faili, F. Ejeckam, J.G. Felbinger, L.F. Eastman, GaN-on-Diamond Field-Effect Transistors: From Wafers to Amplifier Modules, MIPRO, Proceedings of the 33rd International Convention, Opatija, Croatia, May 24–28 (2010) 60–66.

[16] K.K. Chu, P.C. Chao, J.A. Diaz, T. Yurovchak, B.J. Schmanski, C.T. Creamer, S. Sweetland, R.L. Kallaher, C. McGray, G.D. Via, J.D. Blevins, High-Performance GaN-on-Diamond HEMTs Fabricated by Low-Temperature Device Transfer Process, IEEE Compound Semiconductor Integrated Circuit Symposium (CSICS), New Orleans, LA, Oct. 11–14 (2015) 1–4.

[17] C.J.H. Wort and R.S. Balmer, Diamond as an Electronic Material, Materials Today, 11 (2008) 22-28.

[18] Y. Han, B.L. Lau, X. Zhang, Y.C. Leong, K. Fah, Enhancement of Hotspot Cooling with Diamond Heat Spreader on Cu Microchannel Heat Sink for GaN-on-Si Device, IEEE Transactions on Components, Packaging and Manufacturing Technology, 4(6) (2014) 983-990.

[19] A. A. Balandin, S. Ghosh, W. Bao, I. Calizo, D. Teweldebrhan, F. Miao, and C. N. Lau, Superior thermal conductivity of single-layer graphene, Nano Letters, 8(3) (2008) 902-907.

[20] S. Ghosh, I. Calizo, D. Teweldebrhan, E. P. Pokatilov, D. L. Nika, A. A. Balandin, W. Bao, F. Miao, and C. N. Lau, Extremely high thermal conductivity of graphene: Prospects for thermal management applications in nanoelectronic circuits, Applied Physics Letters, 92 (2008) 151911.

[21] M.J. Allen, V.C. Tung, R.B. Kaner, Honeycomb carbon: a review of Graphene. Chem. Rev. 110 (1) (2010) 132–145.

[22] A. Barua, Md.S. Hossain, K.I. Massod and S. Subrina, Thermal Management in 3-D Integrated Circuits with Graphene Heat Spreaders, Physics Procedia, 25 (2012) 311-316.

[23] S.H. Bae, R. Shabani, J.B. Lee and S.J. Baeck, Graphene-Based Heat Spreader on Flexible Electronic Devices, IEEE Transactions on Electron Devices, 26 (2014) 4171-4175.

[24] A. Subrina, D. Kotchethov, A.A. Balandin, Heat Removal in Silicon-on-Insulator Integrated Circuits With Graphene Lateral Heat Spreaders, IEEE Electron Device Letters, 30 (2009) 1281-1283.

[25] S.R. Reddy and G.S. Dulikravich. Analysis of anisotropic graphene platelet heat spreaders to reduce hot spot temperature and temperature non-uniformity, 16th IEEE Intersociety Conference on Thermal and Thermomechanical Phenomena in Electronic Systems (ITherm), 2017, 135-142.

[26] O.A. Williams, Nanocrystalline diamond, Diamond & Related Materials, 20 (2011) 621–640.

[27] D. J. Meyer, T. I. Feygelson, T. J. Anderson, J. A. Roussos, M. J. Tadjer, B. P. Downey, D. S. Katzer, B. B. Pate, M. G. Ancona, K. D. Hobart, and C. R. Eddy Jr., Large-signal RF performance of Nanocrystalline diamond coated AlGaN/GaN High Electron Mobility Transistors, IEEE Electron Device Letters, 35(10) (2014) 1013.

[28] T. J. Anderson, K. D. Hobart, M. J. Tadjer, A. D. Koehler, E. A. Imhoff, J. K. Hite, T. I. Feygelson, B. B. Pate, C. R. Eddy Jr., and F. J. Kub, Nanocrystalline Diamond Integration with III-Nitride HEMTs, ECS Journal of Solid State Science and Technology, 6 (2) (2017) 3036-3039.

[29] M. J. Tadjer, T. J. Anderson, K. D. Hobart, T. I. Feygelson, J. D. Caldwell, C. R. Eddy Jr., F. J. Kub, J. E. Butler, B. Pate, and J. Melngailis, Reduced Self-Heating in AlGaN/GaN HEMTs Using Nanocrystalline Diamond Heat-Spreading Films, IEEE Electron Device Letters, 33 (2012) 23-25.

[30] M. J. Tadjer, T. J. Anderson, T. I. Feygelson, K. D. Hobart, J. K. Hite, A. D. Koehler, V. D. Wheeler, B. B. Pate, C. R. Eddy Jr., and F. J. Kub, Nanocrystalline diamond capped AlGaN/GaN high electron mobility transistors via a sacrificial gate process, Physica Status Solidi A 213 (4) (2016) 893–897.

[31] A.F. Al-Neama, N. Kapur, J. Summers, H.M. Thompson, An experimental and numerical investigation of the use of liquid flow in serpentine microchannels for microelectronics cooling, Applied Thermal Engineering, 116 (2017) 709-723.

[32] A. F. Al-Neama, Z. Khatir, N. Kapur, J. Summers, H. M. Thompson, An experimental and numerical investigation of chevron fin structures in serpentine minichannel heat sinks, International Journal of Heat and Mass Transfer, 120 (2018) 1213-1228.

[33] CREE CGHV1J070D Data sheet, http://www.wolfspeed.com/downloads/dl/file/id/418/product/131/cghv1j070d.pdf, June 2012.

[34] R.H. Shih, P.J. Schilling, Parametric Modeling with SolidWorks 2015, 2015, New Orleans, Louisiana.

[35] S.G. Kandlikar, S. Joshi, S. Tian, Effect of surface roughness on heat transfer and fluid flow characteristics at low Reynolds numbers in small diameter tubes, Heat Transfer Engineering, 24 (3) (2003) 4 – 16.

[36] Y.J. Lee, P.S. Lee, S.K. Chou, Enhanced thermal transport in micro channels using oblique fins, Journal of Heat Transfer 134 (9) (2012) 101901-1-10.

[37] R.J. Philips, Forced-convection, liquid-cooled microchannel heat sinks, Master Thesis, Massachusetts Institute of Technology, Cambridge, MA, 1987.

[38] ASME PTC 19.1-2013 (Revision of ASME PTC 19.1-2005) Test uncertainty, New York, 2013.

[39] H.W. Coleman, W.G. Steele Experimentation, validation, and uncertainty analysis for engineers, 3rd edition, 2009, John Wiley and Son. Inc., Hoboken, New Jersey, USA.

[40] W. Qu, I. Mudawar, Analysis of three-dimensional heat transfer in micro-channel heat sinks, International Journal of Heat and Mass Transfer, 45 (2002) 3973-3985.

[41] Comsol Multiphysics v.5.2, Heat Transfer Module User's Guide, 2015.

[42] C.S. Sharma, M.K. Tiwari, B. Michel, D. Poulikakos, Thermofluidics and energetics of a manifold microchannel heat sink for electronics with recovered hot water as working fluid, International Journal of Heat and Mass Transfer, 58 (1-2) (2013) 135–151.

[43] K. Dhinsa, C. Bailey, K. Pericleous, Investigation into the performance of turbulence models for fluid flow and heat transfer phenomena in electronic applications, IEEE Transactions on Components and Packaging Technologies. 28 (4) (2005) 686-699.

[44] D.C. Wilcox, Turbulence modeling for CFD, Third edition, DCW industries, Inc., La Canada, CA, 2006.

[45] W.M. Kays, Turbulent Prandtl Number — Where Are We?, ASME Journal of Heat Transfer, 116 (1994) 284–295.

[46] Y.J. Lee, P.K. Singh, P.S. Lee, Fluid flow and heat transfer investigations on enhanced microchannel heat sink using oblique fins with parametric study, International Journal of Heat and Mass Transfer, 81 (2015) 325–336.

[47] C.A. Gilkeson, V.V. Toropov, H.M. Thompson, M.C.T. Wilson, N.A. Foxley, P.H. Gaskell, Dealing with numerical noise in CFD-based design optimization, Computers and Fluids 94 (2014) 84–97.

[48] A. Nararyanan, V.V. Toropov, A.S. Wood, I.F. Campean, Simultaneous model building and validation with uniform designs of experiments, Eng. Optim. 39 (5) (2007) 497–512.

[49] V.M.A. Leitão, C.J.S. Alves, C.A. Duarte, Advances in Meshfree Techniques, Springer Netherlands 2007.

[50] K. Deb, A. Pratap, S. Agarwal, T. Meyarivan, A fast and elitist Multiobjective Genetic Algorithm: NSGA-II, IEEE Transactions on evolutionary computation, 6 (2) (2002) 182-197.

[51] A. Abraham, L. Jain, R. Goldberg, Evolutionary multiobjective optimization, Theoretical advances and applications, Springer, 2005.

[52] X. Chen, F.N. Donmezer, S. Kumar, S. Graham, A numerical study on comparing the active and passive cooling of AlGaN/GaN HEMTs, IEEE Transactions on Electron Devices, 61(12) (2014) 4056-4061.

[53] A. Sarua, H. Ji, K.P. Hilton, D.J. Wallis, M.J. Uren, T. Martin, M. Kuball, Thermal boundary resistance between GaN and substrate in AlGaN/GaN electronic devices, IEEE Transactions on Electron Devices, 54(12) (2007) 3152-3158.

[54] A.A. Balandin, Thermal Properties of Graphene and Nanostructured Carbon Materials, Nature Materials, 10 (2011) 569-581.

[55] C. J. Shearer, A. D. Slattery, A. J. Stapleton, J. G. Shapter, C. T. Gibson, Accurate thickness measurement of graphene, Nanotechnology, 27 (2016) 1-10.

Table Captions

Table 1: Uncertainty for various critical parameters of serpentine MCHS.

Table 2: Grid independence tests.

Table 3: Thickness and thermal conductivity of the materials used for simulation.

Table 4: Grid independence tests.

Table 1: Uncertainty for various critical parameters of serpentine MCHS.

Variable	Absolute uncertainties
Channel width (W_{ch})	4 μm
Channel height (H_{ch})	5 μm
Channel length (L_{ch})	15 μm
Fin width (W_w)	3 μm
Hydraulic diameter (D_h)	1.2%
Volumetric flow rate (Q_{in})	0.65 – 1.27%
Temperature (T)	0.3 °C
Pressure drop (ΔP)	3.6 – 9.2%
Thermal resistance (R_{th})	2.8 – 7.3%
Nusselt number (Nu)	3.0 – 6.8%

Table 2: Grid independence tests.

Heat sink model	Grid No.	Number of elements×10^6	$T_{junction}$ (°C)	E%	ΔP (Pa)	E%
Serpentine MCHS	1	1.655	57.9	6.2	6632	7.6
	2	2.269	56.4	3.5	6411	4.0
	3	3.372	55.1	1.1	6243	1.3
	4	4.209	54.5	—	6162	—

Table 3: Thickness and thermal conductivity of the materials used for simulation.

Material	Thickness [µm]	Thermal conductivity [W/(m.K)]	Ref.
Si	100 - 600	$k_{Si} = 152 \times (298/T)^{1.334}$	[18]
SiC	100 - 600	$k_{SiC} = 387 \times (293/T)^{1.49}$	[52]
Diamond	100 - 600	$k_{Diam} = 1832 \times (298/T)^{1.305}$	[18]
GaN	2	$k_{GaN} = 141 \times (298/T)^{1.211}$	[18]
Few-layer graphene	5 - 25	2000	[25]
Cu	2000	385	[18]
80Au/20Sn solder	50	57	[18]
NCD	2	500	[28]
SiN	0.05	15	[28]

Table 4: Grid independence tests.

Heat sink model	Grid No.	Number of elements×10^6	T_{max} (°C)	E%	ΔP (Pa)	E%
Serpentine MCHS	1	2.824	69.12	6.3	26344.8	4.62
	2	3.732	67.38	3.6	26893.6	2.64
	3	5.056	65.70	1.0	27287.3	1.21
	4	6.109	65.04	—	27622.4	—
Straight MCHS	1	2.232	76.20	5.8	108.95	5.50
	2	3.211	74.23	3.1	111.23	3.51
	3	4.546	72.66	0.9	113.77	1.31
	4	5.674	72.01	—	115.28	—

Figure Captions

Fig. 1: Schematic diagram of the experiment setup.

Fig. 2: (a) 3-D isometric actual and top view of a serpentine rectangular MCHS design; (b) Exploded view of serpentine MCHS model, all dimensions in mm.

Fig. 3: 3-D view and back side of serpentine MCHS design used in the simulation; (a) Conjugate heat transfer of the MCHS; (b) Isometric view; (c) Bottom side of the MCHS.

Fig. 4: (a) Pressure drop and thermal resistance; (b) Average Nusselt numbers and average channel base temperature as a function of Reynolds number for serpentine MCHS at input power of 100 W.

Fig. 5: Pareto front showing the compromises that can be struck in minimising both R_{th} and ΔP together with seven representative design points (e.g. P_1 ,…, P_7) used for the MCHS performance analysis.

Fig. 6: (a) Top view of transistor layouts, showing multi-fingered configurations: Source (S), gate (G), and drain (D) metallizations are indicated (all dimensions in µm); (b) 3-D view of the serpentine MCHS design with boundary condition; (c) schematic of GaN HEMT with NCD heat-spreading film; and (d) the finite element mesh using grid 3 as shown in Table 4.

Fig. 7: Validation of the current numerical simulation against experimental work of Han et al. [18] for (a) maximum transistor temperature at different total heating power; (b) temperature distribution along the transistors.

Fig. 8: Effect of the Q_{in} on maximum heater temperature at different heat spreaders (Diamond, SiC and Si) with and without NCD layer, at heat flux of 1823 W/cm^2 and $t_{spreader} = 300\ \mu m$.

Fig. 9: Temperature profile in the longitudinal direction across all gate fingers at heat flux of 1823 W/cm^2, $Q_{in} = 0.10\ l/min$ and $t_{spreader} = 300\ \mu m$.

Fig. 10: Effect of the heat spreader thickness on the thermal performance of the structure for four different heat spreaders (Diamond, SiC and Si), at $Q_{in} = 0.10\ l/min$ and heat flux of 1823 W/cm^2.

Fig. 11: Maximum temperature of the GaN HEMT as a function of the thickness-dependent thermal conductivity of graphene heat spreader, at $Q_{in} = 0.10\ l/min$ and heat flux of 1823 W/cm^2.

Fig. 12: Temperature distribution (°C) at the interface between the heat spreader and GaN HEMT: (a) graphene spreader without NCD layer; (b) diamond spreader with NCD layer; (c) graphene spreader with NCD layer, at 1823 W/cm^2, $Q_{in} = 0.10\ l/min$ and $t_{spreader} = 25\ \mu m$.

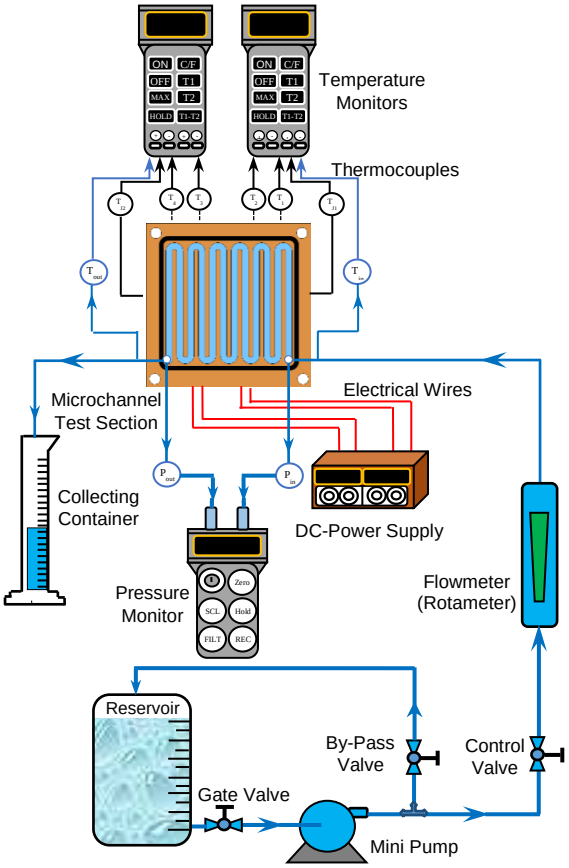

Fig. 1: Schematic diagram of the experiment setup.

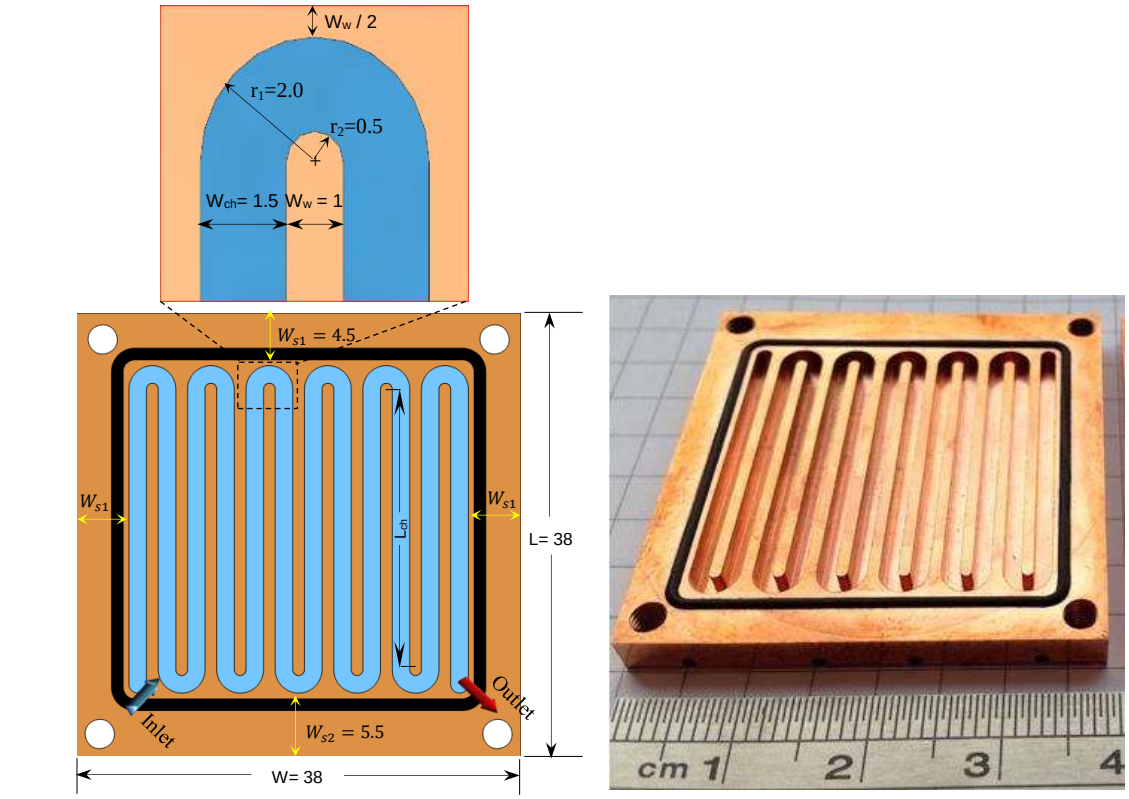

(a)

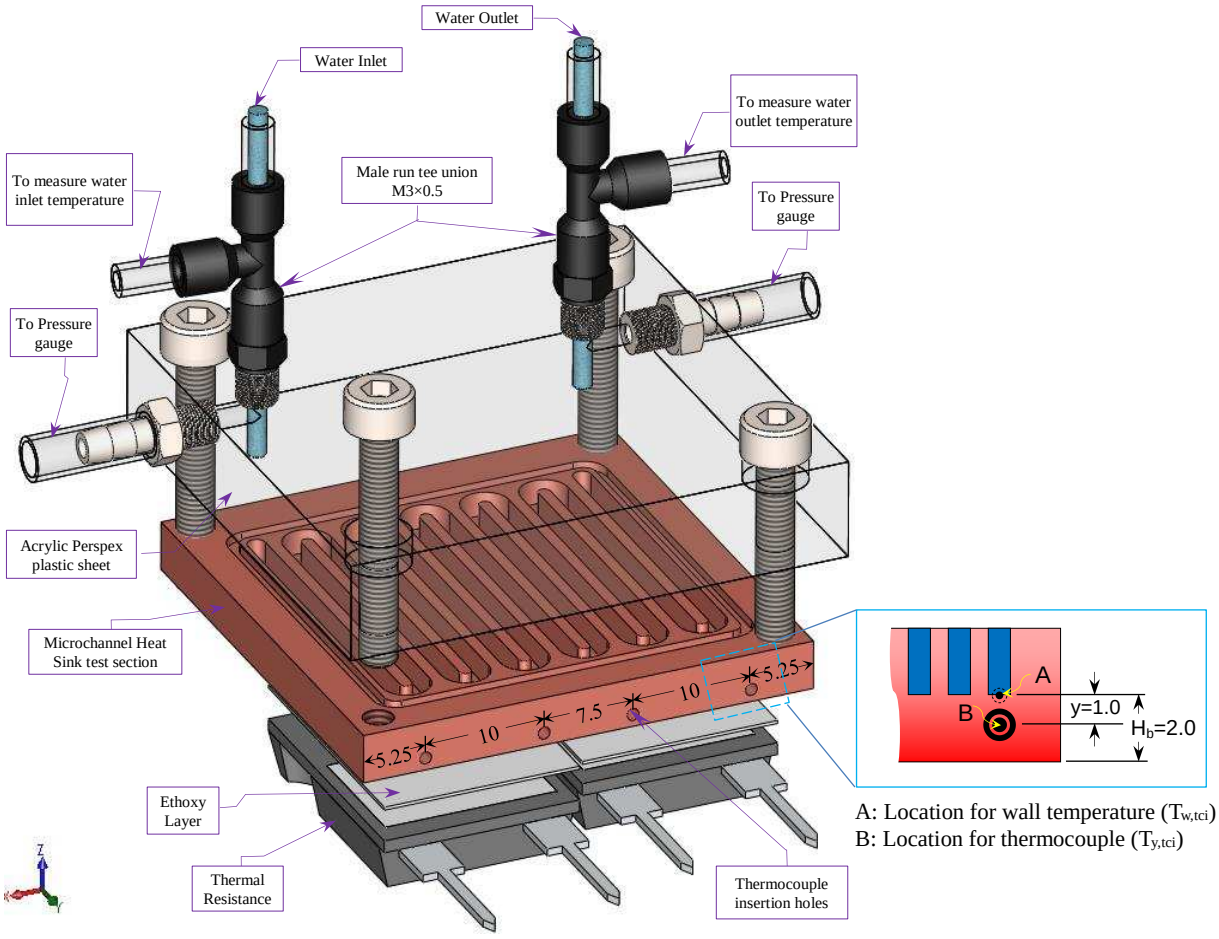

(b)

Fig. 2: (a) 3-D isometric actual and top view of a serpentine rectangular MCHS design; (b) Exploded view of serpentine MCHS model, all dimensions in mm.

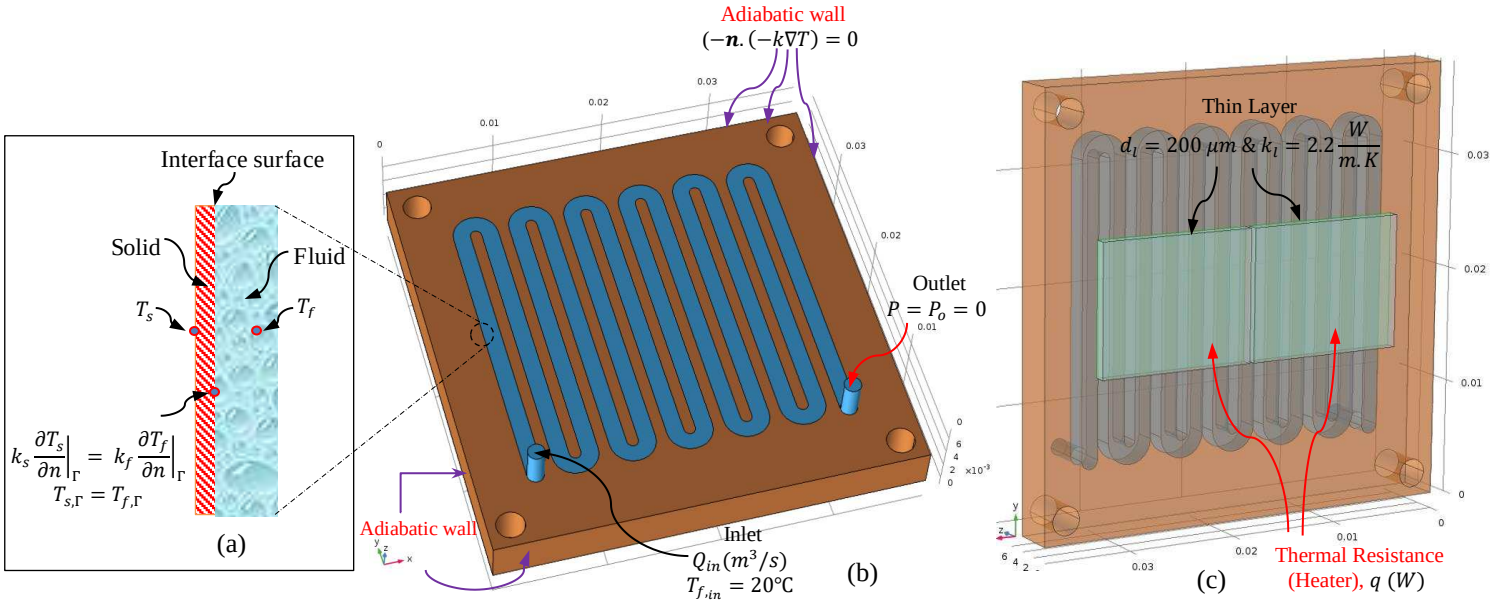

Fig. 3: 3-D view and back side of serpentine MCHS design used in the simulation; a) Conjugate heat transfer of the MCHS; b) Isometric view; c) Bottom side of the MCHS.

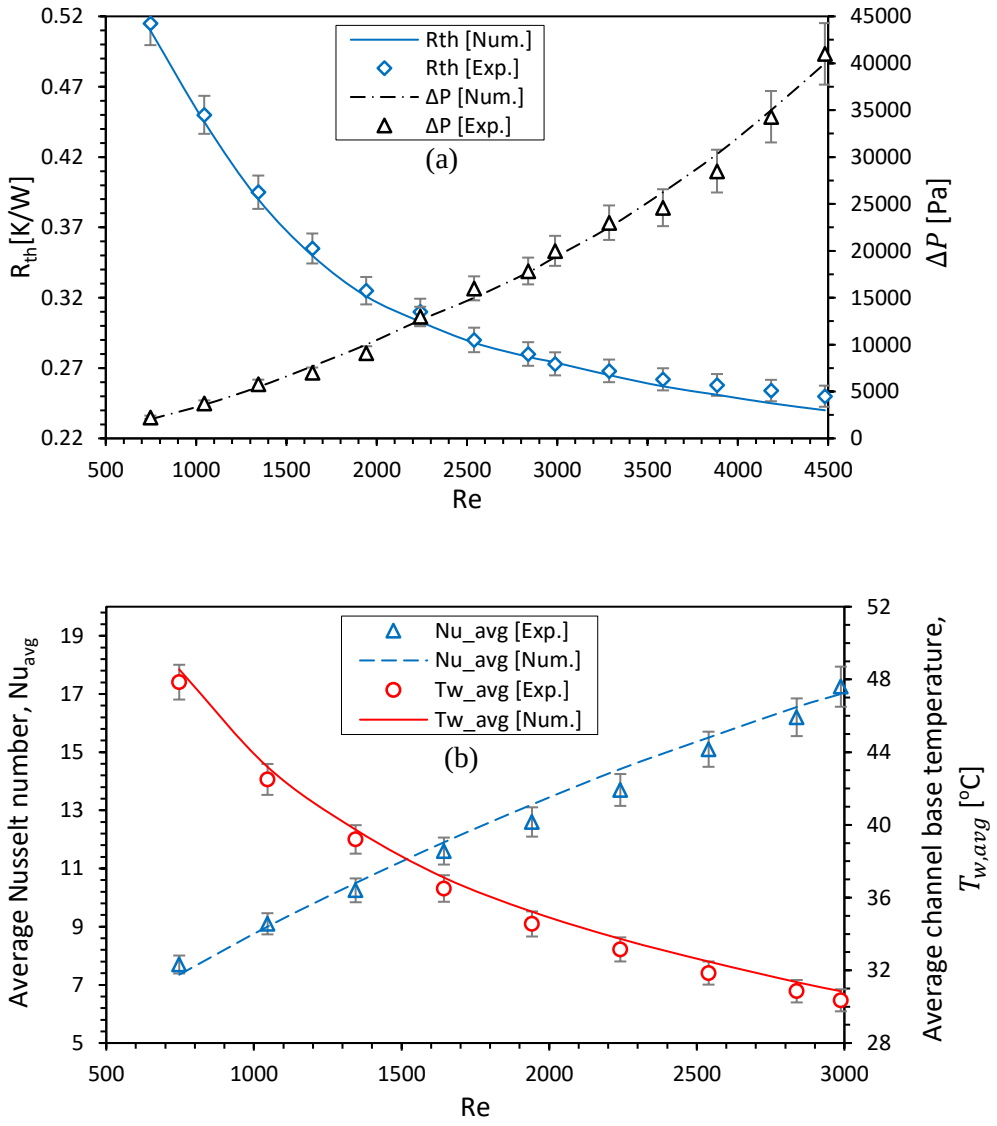

Fig. 4: (a) Pressure drop and thermal resistance; (b) Average Nusselt numbers and average channel base temperature as a function of Reynolds number for serpentine MCHS at input power of 100 W.

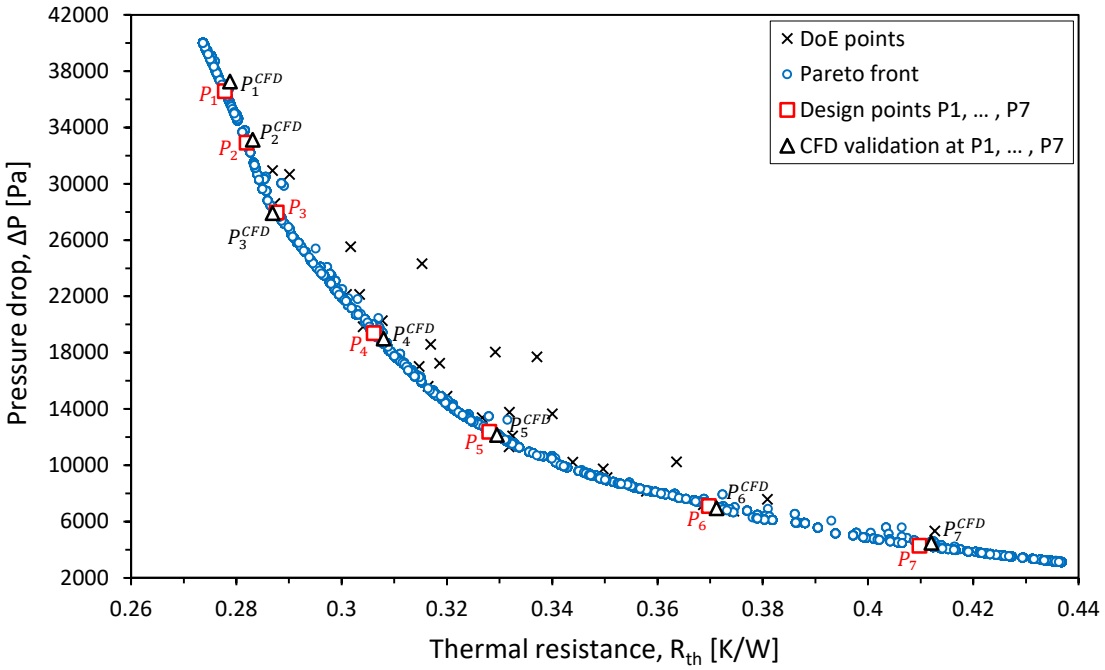

Fig. 5: Pareto front showing the compromises that can be struck in minimising both R_{th} and ΔP together with seven representative design points (e.g. P_1 ,…, P7) used for the MCHS performance analysis.

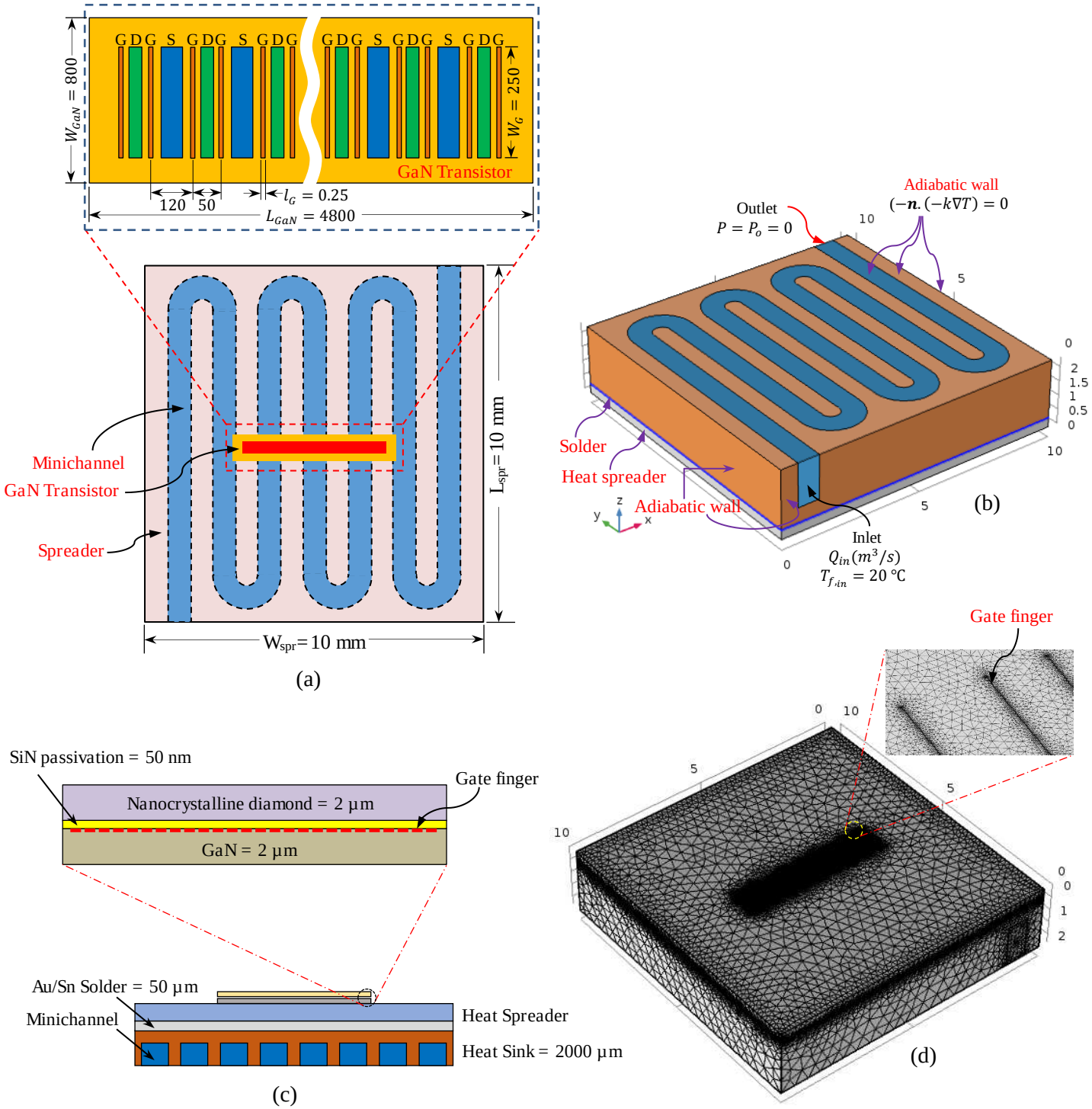

Fig. 6: (a) Top view of transistor layouts, showing multi-fingered configurations: Source (S), gate (G), and drain (D) metallizations are indicated (All dimensions in µm); (b) 3-D view of the serpentine MCHS design with boundary condition; (c) schematic of GaN HEMT with NCD heat-spreading film; and (d) the finite element mesh using grid 3 as shown in Table 4.

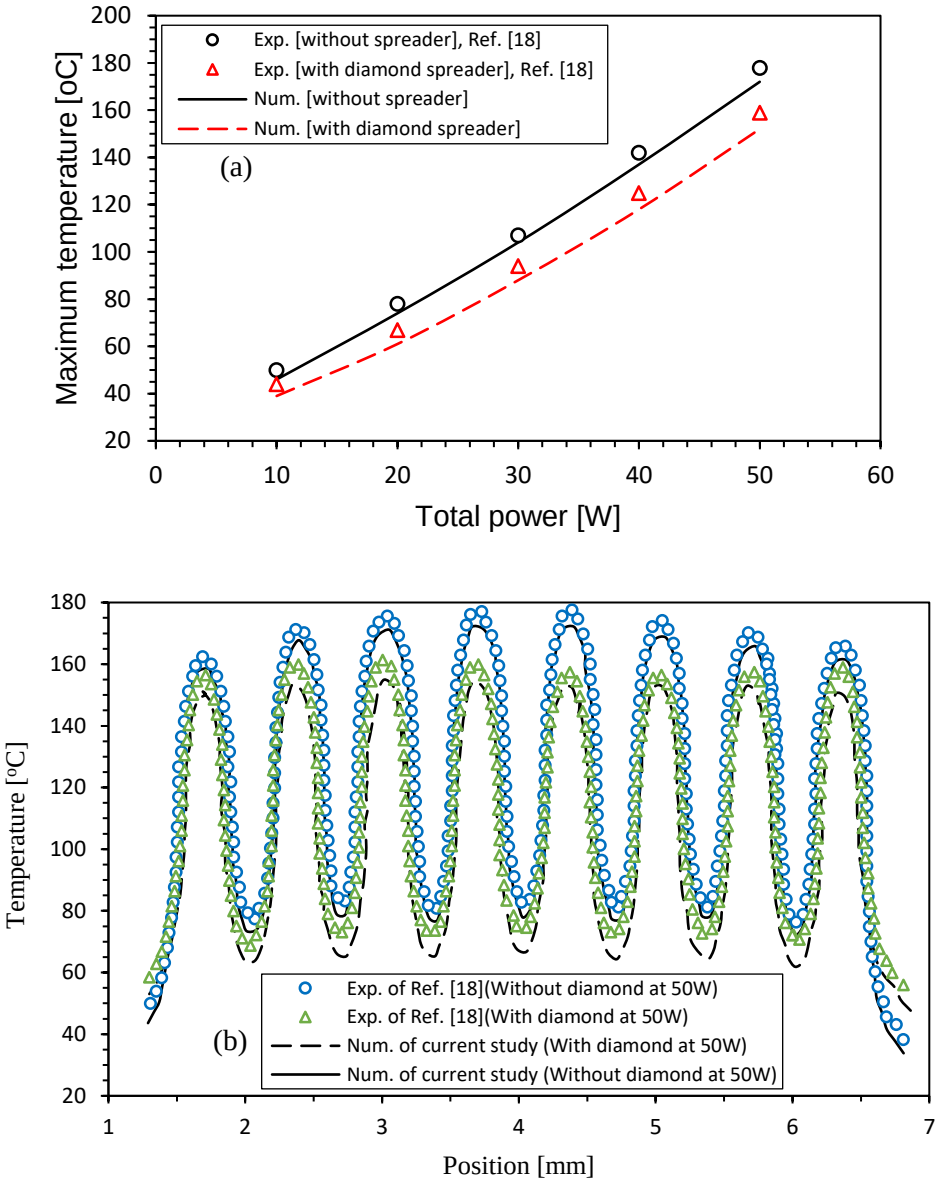

Fig. 7: Validation of the current numerical simulation against experimental work of Han et al. [18] for (a) maximum transistor temperature at different total heating power; (b) temperature distribution along the transistors.

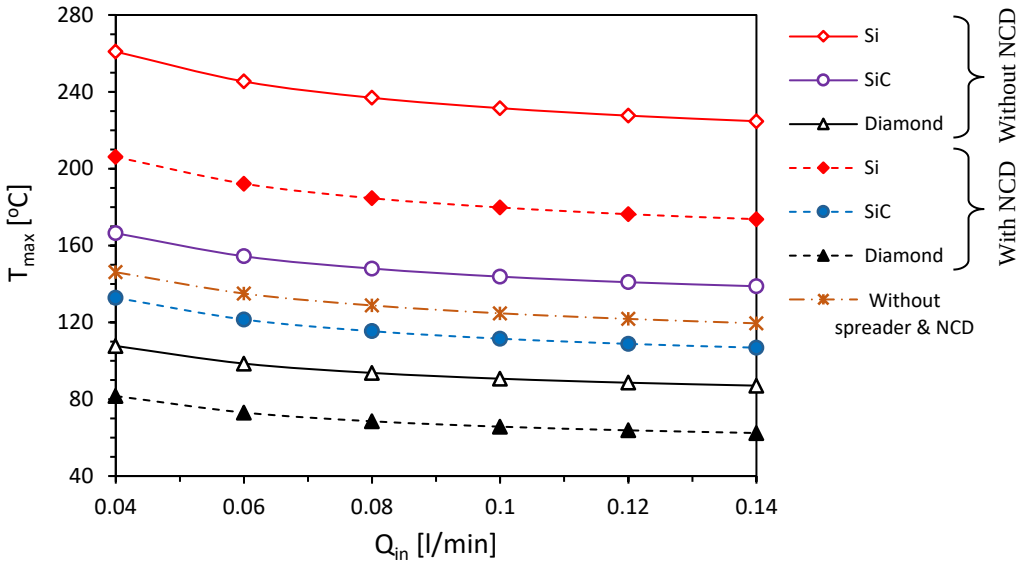

Fig. 8: Effect of the Q_{in} on maximum heater temperature at different heat spreaders (Diamond, SiC and Si) with and without NCD layer, at heat flux of 1823 W/cm^2 and $t_{spreader} = 300\ \mu m$.

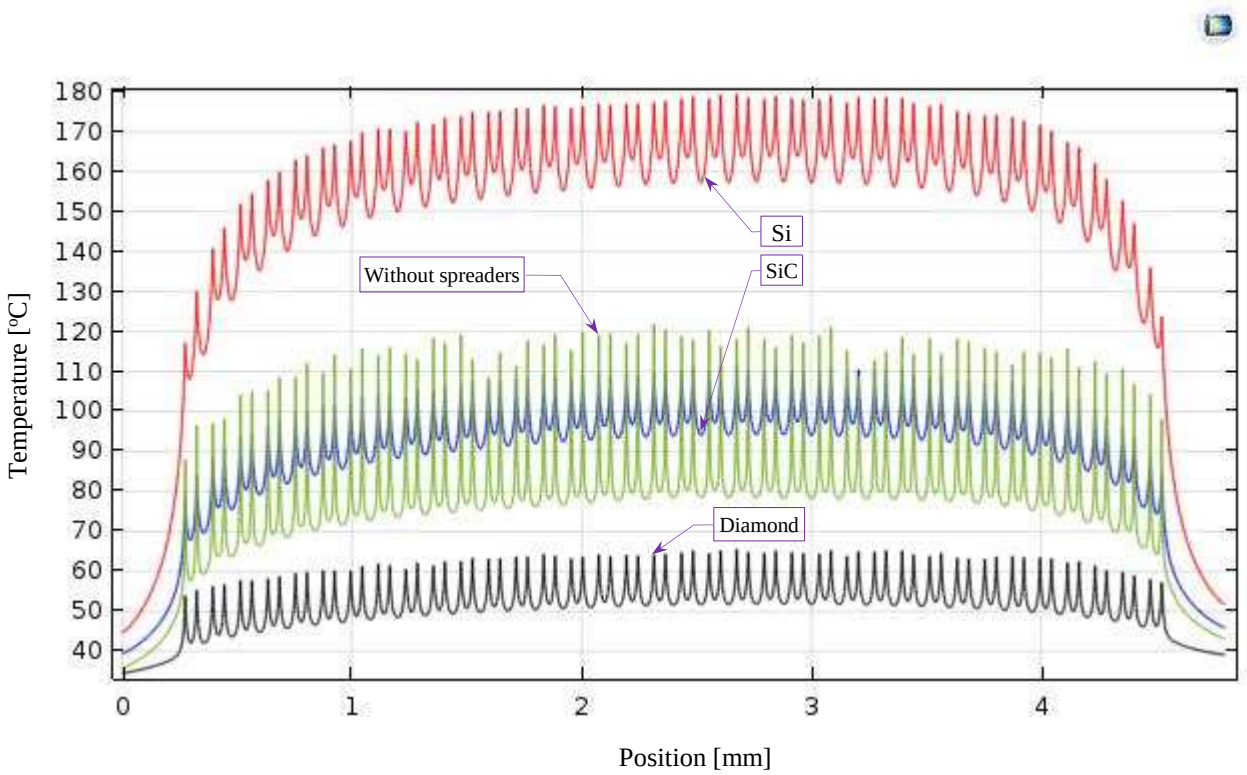

Fig. 9: Temperature profile in the longitudinal direction across all gate fingers at heat flux of 1823 W/cm^2, $Q_{in} = 0.10\ l/min$ and $t_{spreader} = 300\ \mu m$.

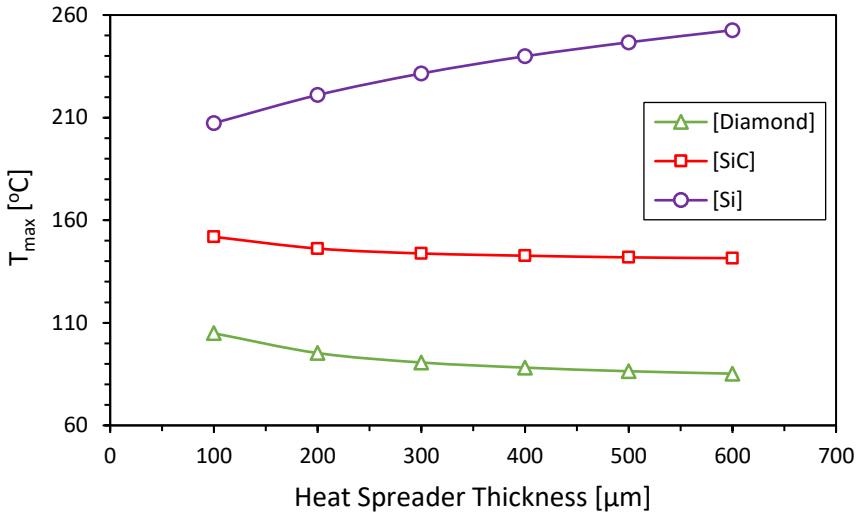

Fig. 10: Effect of the heat spreader thickness on the thermal performance of the structure for three different heat spreaders (Diamond, SiC and Si) without NCD layer, at $Q_{in} = 0.10\ l/min$ and heat flux of 1823 W/cm^2.

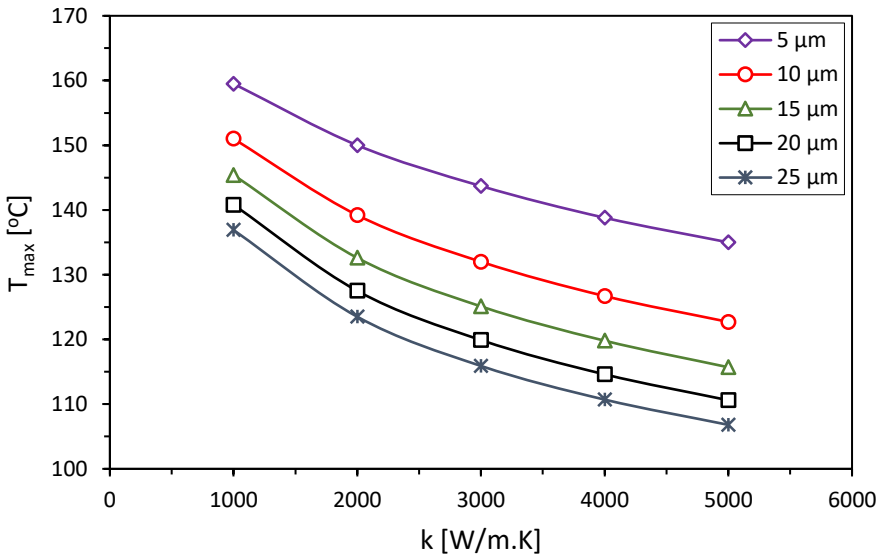

Fig. 11: Maximum temperature of the GaN HEMT as a function of the thickness-dependent thermal conductivity of graphene heat spreader, at $Q_{in} = 0.10\ l/min$ and heat flux of 1823 W/cm^2.

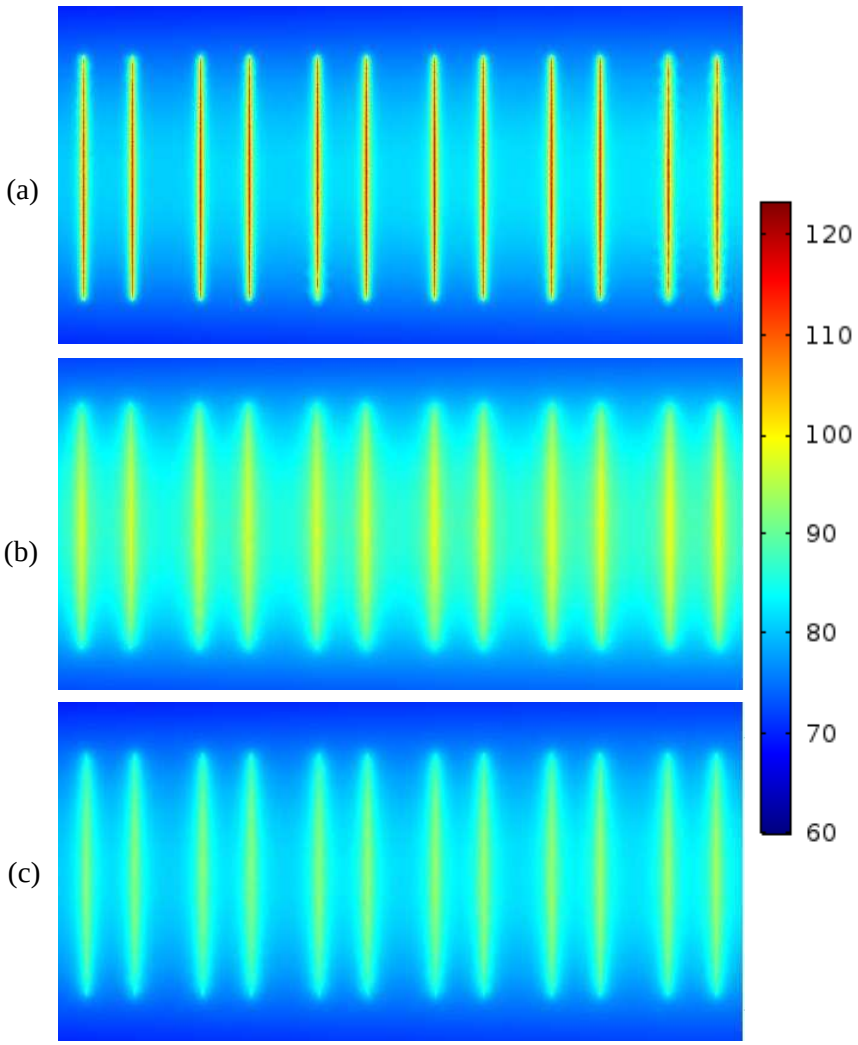

Fig. 12: Temperature distribution (°C) at the interface between the heat spreader and GaN HEMT: (a) graphene spreader without NCD layer; (b) diamond spreader with NCD layer; (c) graphene spreader with NCD layer, at 1823 W/cm^2, $Q_{in} = 0.10\ l/min$ and $t_{spreader} = 25\ \mu m$.